TECHNISCHE UNIVERSITÄT WIEN
Vienna University of Technology

Characterization of the IBA StingRay plane-parallel ionization chamber for proton and carbon dosimetry.

DIPLOMARBEIT

zur Erlangung des akademischen Grades

Diplom-Ingenieurin

im Rahmen des Studiums

Biomedical Engineering

eingereicht von

Viktoria Anna Moser, Bsc
Matrikelnummer 01225497

ausgeführt am Atominstitut an der Fakultät für Physik

der Technischen Universität Wien

Betreuung:
Univ.Prof. Dipl.-Ing. Dr.techn. Dietmar Georg
Mag. Peter Kuess, PhD
Hugo Palmans, MSc,PhD

Wien, 17. Oktober 2021

Viktoria Anna Moser | Dietmar Georg

Acknowledgements

First of all I want to thank Univ.Prof. Dipl.-Ing.Dr.techn.Dietmar Georg for the supervision and for the possibility to work at MedAustron.

Secondly, a big thanks to my co-supervisor Mag. Peter Kuess, PhD, who supported me a lot and helped to motivate me during the global pandemic. He stayed positive and showed an abundance of patience throughout the process of this thesis.

Thirdly, I want to thank Hugo Palmans, MSc,PhD for sharing and supporting with his great know-how and good discussions.

Moreover I want to thank Dr.Monika Clausen for introducing me into MedAustron and supervising me the first few months, DI Dr. Albert Hirtl for mediation of the supervisor and Severine Rossomme,PI from IBA for the possibility to work with the IBA equipment.

Last but not least, I want to express my gratitude to my family and all my friends for their encouragement and great support.

Kurzfassung

Der Hersteller IBA (IBA Dosimetry GmbH, Schwarzenbruck, Deutschland) entwickelte eine neue großflächige plan-parallele Ionisationskammer, die IBA StingRay, mit einem Durchmesser von 156 mm und einem vom Hersteller angegebenen aktiven Durchmesser von 120 mm. Im Rahmen dieser Arbeit wurden verschiedene Messmethoden mit Schmalstrahl Photonen, Protonen und Kohlenstoffionen durchgführt, um die laterale Dosisantwort der StingRay mit Seriennummer SN91 und SN93 zu messen und die Messmethoden zu vergleichen.

Demnach wurden von der IBA StingRay Kammer horizontale und vertikale Profilmessungen mit Röngten und Protonenstrahlung gemacht sowie diagonale Profilmessungen mit Photonenschmalstrahlung.

Die Ergebnisse beider IBA StingRay Kammern der horizontalen Profilmessung mit Photonenstrahlung zeigten eine um zirka 5% erhöhte gemessene Ladung der Kammer bei einen Radius von ±25 mm bis ±60 mm im Vergleich zu der Ladung im Zentrum der Kammer. Die vertikale Profilmessung der IBA StingRay Kammern mir Photonenstrahlung zeigte diesen Anstieg nicht. Die vertikalen und horizontalen Profilmessungen mit Protonenstrahlung lieferten ähnliche Ergebnisse zu den Messungen mit Photonenstrahlung, allerdings kam es hier bei der horizontalen Profilmessung nicht,wie bei den Messungen mit der Photonenstrahlung, zu so einem signifkanten Anstieg im äußeren Kammerradius. Des Weiteren wurde eine vollständige Profilrastermessung von einem Raster der Größe 70 mm x 70 mm mit Photonenschmalstrahlung durchgeführt und analysiert. Hier sah man, dass die IBA StingRay Kammer mit Seriennummer 93 über alle Messpunkte hinweg um zirka 2% homogener war, als die Kammer mit Seriennummer 91.

Außerdem behandelt diese Arbeit die Polarität, Dosisstabilität, Dosisrate und Spannungsstabilität mit Photonenschmalstrahlung der IBA StingRay plan-parallelen Ionisationskammer mit Seriennummer SN91. Hier gab es keine Auffälligkeiten. Die Polarität war bis zu 1.12% hoch, die Dosisstabilität und Dosisrate wies ein lineares Verhältnis auf und die Spannungsstabilität war quadratisch.

Des Weiteren wurde der Ionen-Rekombinationseffekt, der IBA StingRay plan-parallelen Ionisationskammer mit Kohlenstoffionenstrahl gemessen.

Der Ionen Rekombinationseffekt wurde mit verschiedenen Kohlenstoffionenstrahlenergien im Plateau, Peak und Abfall des Strahls gemessen. Weiters wurde die IBA StingRay Ionisationskammer mit verschiedenen Spannungen im Bereich von -150 V bis zu 150 V versorgt und deren Ladung dazu gemessen. Außerdem wurden Messungen mit und ohne Ripple Filter für verschiedenene Strahlintensitäten durchgeführt. Es wurde das Rekombinationsverhalten bei verschiedenen lateralen Verschiebungen ($\pm$30 mm) gemessen und analysiert.

Die Ergbenisse im Bragg Peak zeigten, dass die initiale Rekombination bei maximal 1.5% liegt sowie die Volumsrekombination bei maximal 0.2%.

Zusammenfassend war das Verhalten beider IBA StingRay Kammern (SN91 und SN93) sehr ähnlich. Im Vergleich zu anderen Ionisationskammern, wie zum Beispiel der PTW 34089, war die Ionisationskammerladung der IBA StingRay allerdings deutlich geringer als die der PTW34089.

Abstract

The vendor IBA (IBA Dosimetry GmbH, Schwarzenbruck, Deutschland) has developed a new large area plan-parallel ionisation chamber, the so called IBA StingRay chamber, with an outer diameter of 156 mm and a nominal diameter of the active area of 120 mm.

Different methods to measure a lateral dose response profile of a plane-parallel ionisation chamber were executed with the IBA StingRay chamber and compared within this thesis. Horizontal and vertical profile measurements with photon and proton beams as well as a diagonal profile measurement with photon beam were performed.

The horizontal response of both IBA StingRay chambers (SN91 and SN93) with X-Ray beam showed an increase of the chamber charge of 5% from chamber radius ±25 to ±60 in comparison to the charge at the center. The vertical profile of IBA StingRay chambers in the X-ray beam had no increase towards the edges like that one of the horizontal axis. The results of vertical and horizontal axis of IBA StingRay SN91 with proton beam were similar to the measurements with X-ray beam, except for the increase at the horizontal axis, which occurred for X-ray beam. Moreover a field of 70 mm x 70 mm was measured with a photon beam. The results of this measurements showed that the chamber dose profile of IBA StingRay SN91 and SN93 were similar, but the chamber response of IBA StingRay SN93 was over all measurement points about 2% higher.

Furthermore the polarity, dose stability, dose rate stability and voltage stability of IBA StingRay were measured with X-ray beam. The ion recombination effect of the IBA StingRay were measured with a carbon ion beam.

The polarity of IBA StingRay chamber SN91 had a maximum of 1.12%, the relationships of dose stability as well as dose rate stability were linear and the voltage stability was quadratic.

The ion recombination effect was measured with different carbon ion beam key energies at the plateau, in peak and fall off. Moreover different chamber voltages from -150 V up to 150 V were applied to the IBA StingRay chamber and its corresponding response measured. Measurements with and without ripple filter and different degrader

settings were gathered and analyzed. Last but not least also lateral offsets (±30 mm) were applied to the chamber location. The initial recombination had a maximum of 1.5% and the volume recombination was maximal 0.2% at the bragg peak.

In summary was the behaviour of IBA StingRay chamber SN91 and SN93 very similar. If the IBA StingRay chamber is compared with PTW 34089, it showed that the Ionization chamber charge of IBA StingRay was lower than the Ionization chamber charge of PTW 34089.

Contents

CHAPTER 1

Introduction

The introduction includes a short description about the basics of radiotherapy and has its focus on particle therapy and its physical principles. Moreover detectors, which are used in particle therapy, with main focus on large area plane-parallel ionisation chambers will be presented. Last but not least the chapter includes a short presentation of the MedAustron particle therapy facility.

1.1 Basics of Radiotherapy

Radiotherapy is based on ionizing radiation and its interaction with matter. Of basic interest is the absorbed dose, delivered to the patient, which should be known accurately so that the patient is receiving the correct amount of radiation to kill the cancer cells while at the same time it does not harm any healthy tissue[48]. The type of the radiotherapy is depending on the position of the radiation source in relation to the patient and can be divided in following three types:

- external beam radiotherapy or teletherapy (EBRT)
- brachytherapy or sealed source radiotherapy
- unsealed source radiotherapy

In external beam radiotherapy (EBRT) the radiation source is located outside the patient. The most common radiation types are photons with energies ranging from 200 kV up to 25 MV, which can be produced in conventional X-ray-tubes, in linear accelerators (LINAC) or are emitted by radioisotopes like 60Co. Nowadays EBRT is mostly based on LINACs, which are used because of their accurate and effective photon beam production. LINACs are accelerating electrons towards a metal target, which are losing kinetic energy

when hitting the target. This results in emission of so called Bremsstrahlung, which is used for the radiotherapy. An initial build up to a maximum value, which is followed by an exponential decrease, characterizes the depth-dose profile of photons (see figure 1.1).

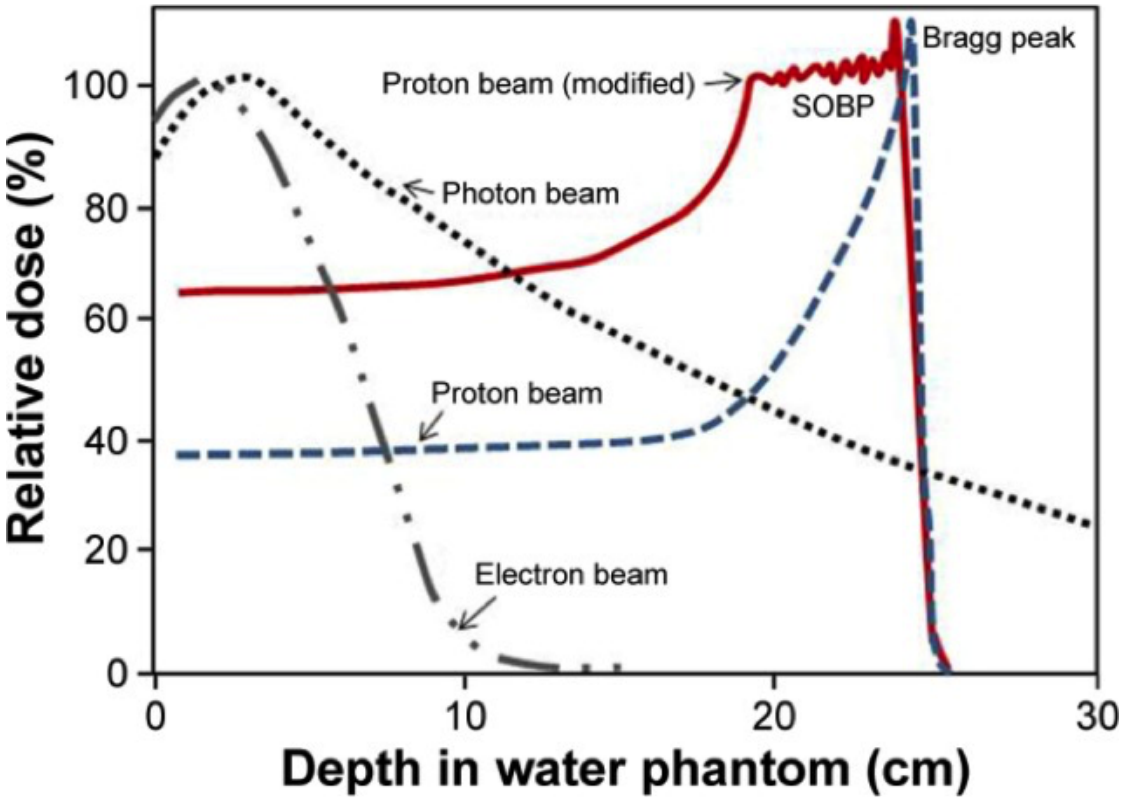

Figure 1.1: Depth-dose profile for photons, electrons and protons[50]

Charged particles like for example electrons, protons or carbon ions are also used in external beam radiotherapy. The electron beam is beneficially used for superficial tumor treatment or during intra- operative electron radiotherapy. Profound tumors are treated with light-ions like protons and carbon ions, due to their depth dose profile. The different depth-dose profiles but not carbon ions are shown in figure 1.1 [49].

1.2 Particle therapy

Particle therapy characterizes the use of ion beams (protons or ions) for the patient treatment of tumors [7].

The main advantage of particle therapy is the reduced dose to normal healthy tissues during radiotherapy in comparison to photons [11].

Ionization and atomic excitation is primarily accomplished if charged particles lose energy by inelastic collisions with atomic electrons. For charged particles (except for electrons), the mean ionization energy loss, or in other words the electronic stopping power (SP), is described by growing energy loss with decreasing particle velocity which causes the characteristic Bragg peak (see figure 1.1). The form of the Bragg peak is not completely sharp, because of range straggling, which means that the actual range of each single particle deviates from the expected mean value [17]. The advantage of the Bragg peak is that unlike to X-rays, the energy deposited per unit track increases with depth, consequently the dose to normal healthy tissue is lower than for photons, when delivering the same dose to the tumor [11]. This irradiation coverage is achieved longitudinally by superimposing different beams with slightly different energies. This generates a Spread Out Bragg Peak (SOBP), which deposits the wanted target dose in tumor treatment[17].

1.3 Interaction of photon radiation with matter

There are different types of interaction with matter and photon radiation:

- Compton effect
- Photo-electric effect
- Pair production
- Rayleigh (coherent) scattering
- Photonuclear interactions

The first three mentioned interactions are the most relevant, because they lead to transfer of energy to electrons, which consequently impart that energy to matter in many Coulomb-force interactions along their tracks [4].

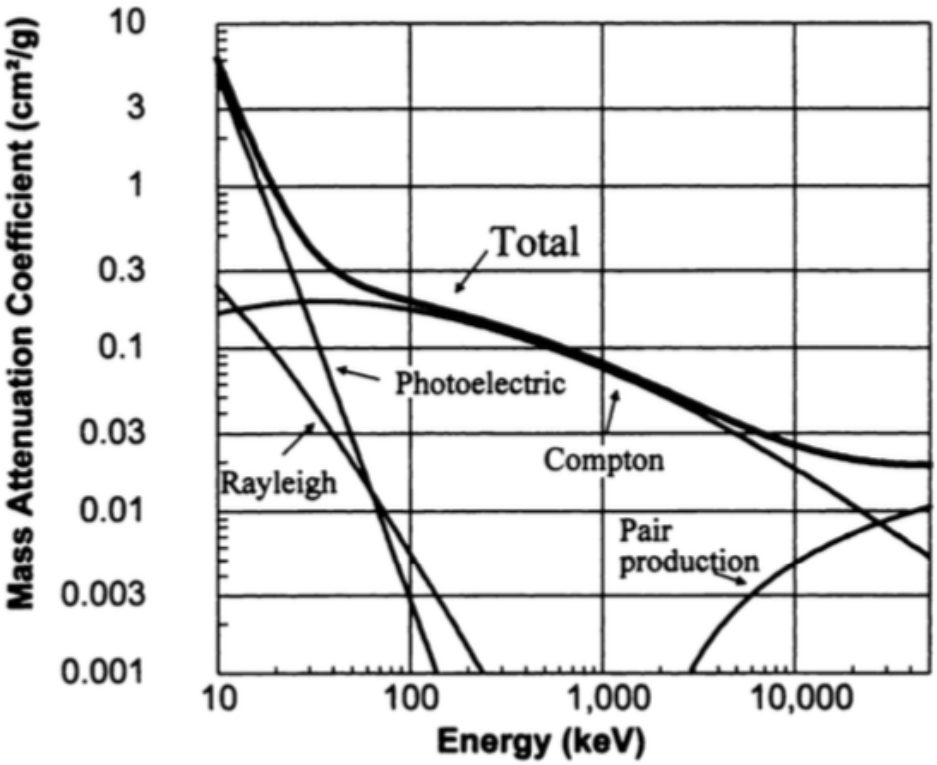

Figure 1.2: Various interactions of photons with matter as a function of energy for soft tissue [28]

Figure 1.2 indicates the various interactions of photons with matter as a function of energy for soft tissue.

1.3.1 Compton effect

The Compton effect as well as the factors that contribute to its probability of occurrence are essential to medical imaging [28].
It is defined as X-ray photons interaction with free or valence shell electron, where the incident photon energy exceeds the binding energy of the valence shell electron, which is consequently ejected. The geometrical arrangement is shown in figure 1.3, where the incident photon with energy $h\nu$ collides with the electron and is scattered with angle θ and energy $h\nu'$. The recoil electron has an angle ϕ and kinetic energy T_e [10].
The relation of the ratio of scattered photon energy $h\nu'$ to incident photon energy $h\nu$ is

obtained as:

$$\frac{h\nu'}{h\nu} = \frac{1}{1+\alpha(1-cos\theta)} \tag{1.1}$$

The variable α represents a dimensionless ratio $h\nu/m_0c^2$ and the relationship between the scattered photon angle is:

$$cot\phi = (1+\alpha)tan(\frac{\theta}{2}) \tag{1.2}$$

The kinetic energy of the scattered electron is obtained by [10]:

$$T_e = h\nu - h\nu' = \frac{\alpha(1-cos\theta)h\nu}{1+\alpha(1-cos\theta)} \tag{1.3}$$

The Compton effect is predominant for energy of x rays from approximately 30 keV to 30 MeV[28].

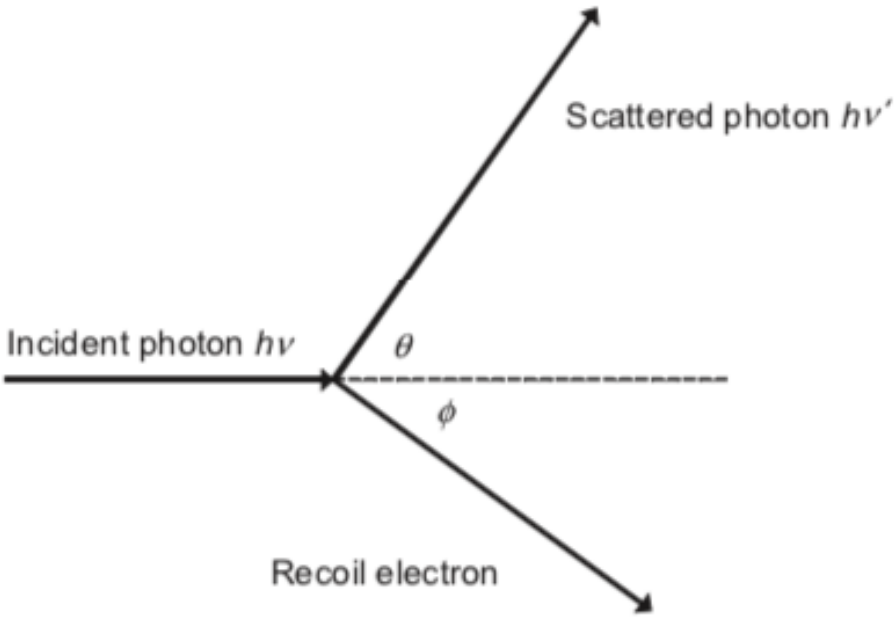

Figure 1.3: Compton effect [10]

1.3.2 Photo-electric effect

The photo-electric effect is defined as the interaction which results in an excited atom and the excess energy is released by ejection of one of the electrons bound to nucleus. The ejected electron is called a photoelectron. The kinetic energy of the electron T is

based on the binding energy of the electron shell from which the electron came E_s and the photon energy $h\nu$:
$T = h\nu - E_s$
The photo-electric effect only happens if the photon energy $h\nu$ exceeds the binding energy of the shell electron. The electron with the highest binding energy is most probable to lose the shell. A vacancy is left in the atomic shell after the photo-electric interaction. This vacancy is filled by an electron from higher shell and the resulting energy difference is carried off by characteristic X-ray radiation or by an Auger electron, which is a another electron from a highers shell.
The schematic representation of the photo-electric effect is shown in figure 1.4 [33].

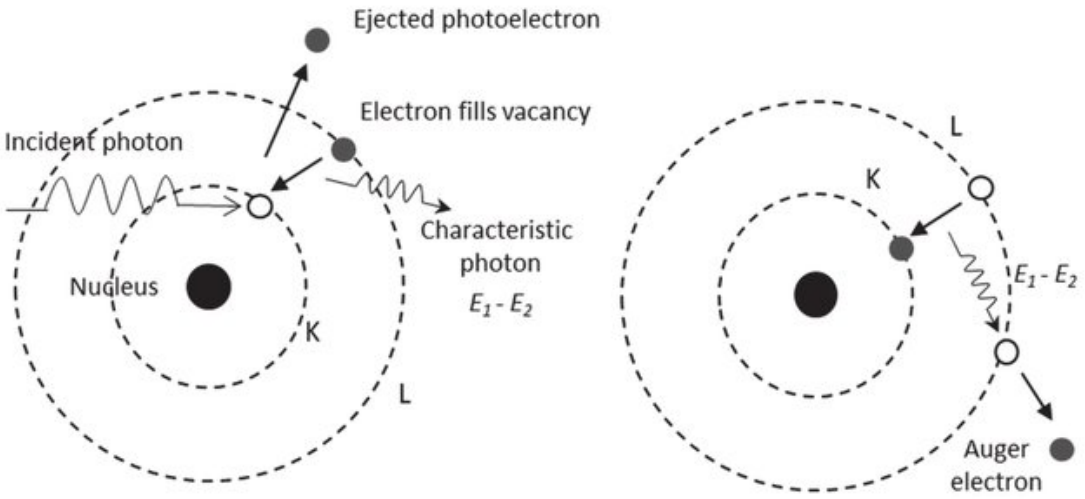

Figure 1.4: Schematic representation of photo-electric effect [33]

If the initial vacancy is filled, the new vacancies will be filled themselves. This process leads to a cascade of events which may leave the atom in a ionized state at the end. The probability of the photo-electric effects highly depends on atomic number and it has a strong inverse dependence on photon energy. The photo-electric effect is predominant for energy of X-rays up to 150 keV and the energy range where it is dominant is strongly Z-dependent [10].

1.3.3 Pair production

Pair production is defined as an interaction of a high energy photon, which passes near an atomic nucleus, with the nuclear coulomb field. If the photon energy exceeds an energy threshold of $2m_0c^2$ (1022 keV), the photon is converted into an electron-positron pair, each with its own kinetic energy[10]. A schematic representation of pair production is shown in figure 1.5 [1].

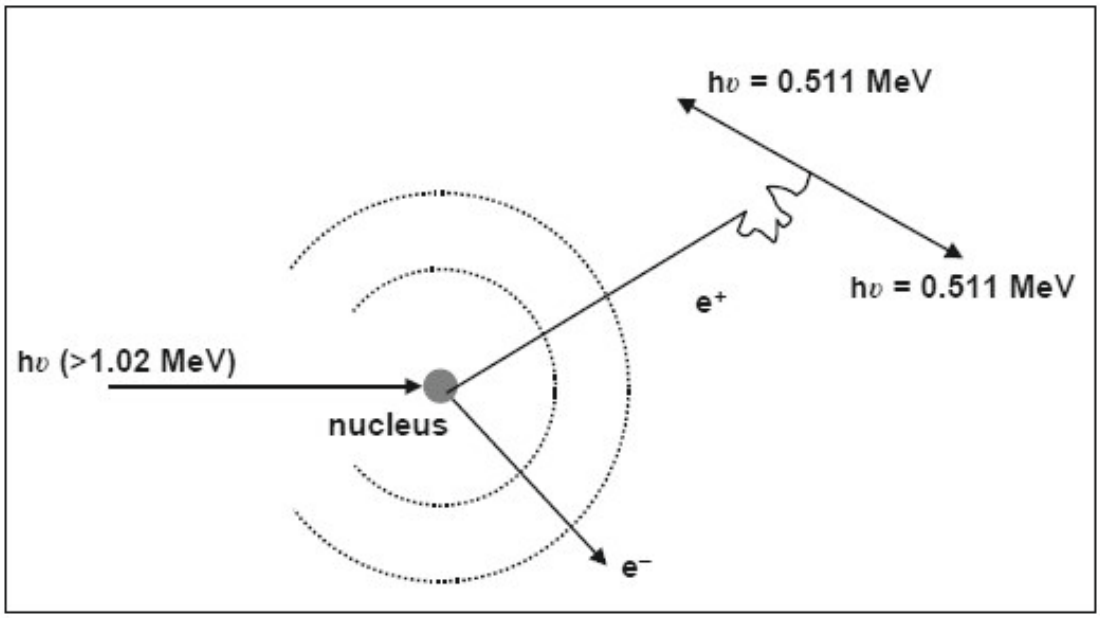

Figure 1.5: Schematic representation of pair production[1]

Pair production cannot take place if the energy of the photons is less than 1022 keV. The process may also occur in the electron field, in this case it is called triplet production, because the target electron itself is ejected with high energy. The photon energy thresholds of pair and triplet productions are much higher than the energy ranges of diagnostic radiology[10].

1.3.4 Rayleigh (coherent) scattering

Rayleigh scattering is defined as coherent scattering where the photon is scattered by the combined action of the whole atom and it is an elastic process because the photon does not lose any energy. Rayleigh scattering does not effect the dose or produces any ionization or excitation, but the atom conserves momentum and the photon is redirected through a small angle. Therefore this effect can be detected in narrow- beam geometry[4].

1.3.5 Photonuclear interaction

The photonuclear interaction is defined as the interaction of an energetic photon, which is exceeding a few MeV, which enters and excites the nucleus. In this case a proton or neutron is emitted by the nucleus[4].

1.4 Interaction of charged particles with matter

A charged particle is surrounded by its Coulomb electric force field, which interacts either with one or more electrons or with the nucleus of the atom it passes. These interactions leads to an energy transfer from charged particles to the electrons or nuclei of the medium.

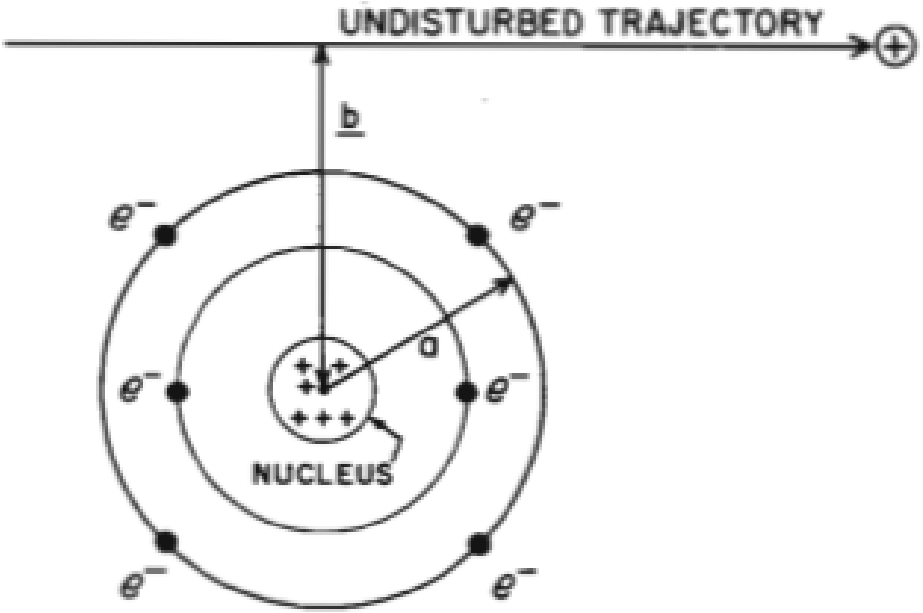

Figure 1.6: Important parameters in charged particle collisions with atoms [4]

The interaction of charged particles by coulomb force can be characterized in terms of the relative size of classical impact parameter b versus the atomic radius a, which is shown in figure 1.6 [4]. The following three types of interaction are dominant:

- "Soft" Collisions ($b \gg a$)
- Hard (or "Knock-On") Collisions ($b \tilde{} a$)
- Coulomb-Force Interaction with the External Nuclear Field ($b \ll a$)
- Nuclear Interactions by Heavy Charged Particles

1.4.1 "Soft" Collisions ($b \gg a$)

The charged particle interacts with the whole atom and the whole atomic complement of bound electrons, if the impact parameter b is much larger than the radius a of the absorber atom. This interaction is known as soft or distant collision. A very small energy transfer

from charged particle to a bound electron happens. This type of interaction happens very often, so that about the half of total energy loss by charged particles happens due to this small- energy transfer interactions, which could lead to atomic polarization, excitation or ionization by removal of a valence electron. All types of charged particles including electrons and positrons undergo soft collisions [43].

1.4.2 Hard (or "Knock-On") Collisions ($b \tilde{} a$)

If the impact parameter b is of the same order as the atomic dimensions, it has a higher probability that the incident particle will firstly interact with a single atomic electron. This electron is then ejected from the atom with kinetic energy and is called a *delta* ray. The *delta* rays are energetic enough to undergo separate additional Coulomb-force interaction and it dissipates its kinetic energy on its own track. The effect of hard collisions depends on the particle type, which is different especially for electrons in comparison to heavy particles. The probability that hard collisions occur depends upon quantum mechanical spin and additional exchange effects, which involves the nature of the incident particle. The number of hard collisions is low in comparison to soft collisions, but the fractions of the primary particles' energy, which are spent by these two processes are comparable. Whenever an inner-shell electron is ejected from an atom because of a hard collision, characteristic X-rays or Auger electrons will be emitted, like it happens if the electron had been removed by photo-electric interaction [4].

1.4.3 Coulomb-Force Interaction with the External Nuclear Field ($b \ll a$)

The Coulomb-force interaction mainly takes place with the nucleus, if the impact parameter b is much smaller than atomic radius a, which is especially important for electrons and heavy charged particles. The electron is scattered elastically and does not emit any X-ray photon or excite the nucleus, in almost all but 2-3% of the encounters. So it is not a mechanism for energy transfer to absorbing medium, but it is important for deflecting electrons. In the other 2 to 3% of the encounters, the electron passes near nucleus and an inelastic radiative interaction occurs, which leads to an emission of an X-ray photon. In this case the electron gives a huge fraction of its kinetic energy to the photon and the electron is not only deflected. This kind of X-rays are called "Bremsstrahlung" [4].

1.4.4 Nuclear Interactions by Heavy Charged Particles

An inelastic nuclear interaction may happens if the impact parameter b is less than the nuclear radius a and if the heavy charged particle has sufficiently high kinetic energy. An intranuclear cascade process happens and collimates in forward direction, if one or more individual nucleons are struck. So called evaporation particles, which are mostly nucleons with low energy, and *gamma*-rays emit, if the highly excited nucleus decays from its excited state. If nuclear interactions are present, the spatial distribution of the absorbed dose is changed, because otherwise some of the kinetic energy would be

deposited as local excitation or ionization, which is carried by neutrons, *gamma*- rays, secondary protons and other charged fragments [4].

1.5 Interactions of ionizing radiation with biological cells

There are only two possibilities of interactions of ionizing radiation with biological cells:

- Direct interaction
- Indirect interaction

1.5.1 Direct interaction

A cell's DNA or proteins are hit by ionizing radiation directly, which affects the cell as a whole and either killing the cell or mutating the DNA. A human has 23 pairs of double-stranded chromosomes. Some cells react like single- stranded DNA and nonpaired chromosomes, which are more radiosensitive. There are many different types of direct hits, the type of damage that occurs determines whether the cell can repair itself or not. The cell dies immediately or is likely to die, if a direct hit causes a complete break in DNA or some other permanent damage. Nevertheless, a replacement of the cell that dies happens if an abundance of cells and somatic cell reproduction happens. Radiation effects are present if the system of replacing cells falters due to higher doses of radiation. Moreover cells are more radiosensitive if they are actively dividing. Cells are reproduced in the 4 phases of mitosis:
The first phase is the so called M (=Mitosis) phase, where the cells divide in two cells. The second phase is the $G1$ phase, here the cells prepare for DNA replication. The third phase is the S (=Synthesis) phase in which the DNA doubles by replication. The last phase is the $G2$ phase, in which cells prepare for mitosis. The most radiosensitve phase of the four mentioned phases is the M phase, in which the chromosomes condenses and pairs. Cancer cells have an increased amount of chromatin and have unusually high mitotic rates, that are more radiosensitive than normal cells [6].

1.5.2 Indirect interaction

If radiation energy is deposited in the cell and the radiation interacts with cellular water rather than with the macro molecules like DNA or proteins, the interaction is called indirect cellular interaction. In this case the reaction of the interaction is hydrolysis of the water molecule, which results in to a hydrogen molecule and free radical hydroxyl molecule. If a recombination of two hydroxyl molecules happens, other reactive oxygen species are formed that combines with some organic compounds, which further combines within the cell to form an stable organic hydrogen peroxide molecule. This process can cause to a loss of crucial enzymes in the cell, which further results into cell death or future mutation of the cells. There has been much research, to block free radical hydroxyl recombination into hydrogen peroxide, to prevent the occurrence of stable

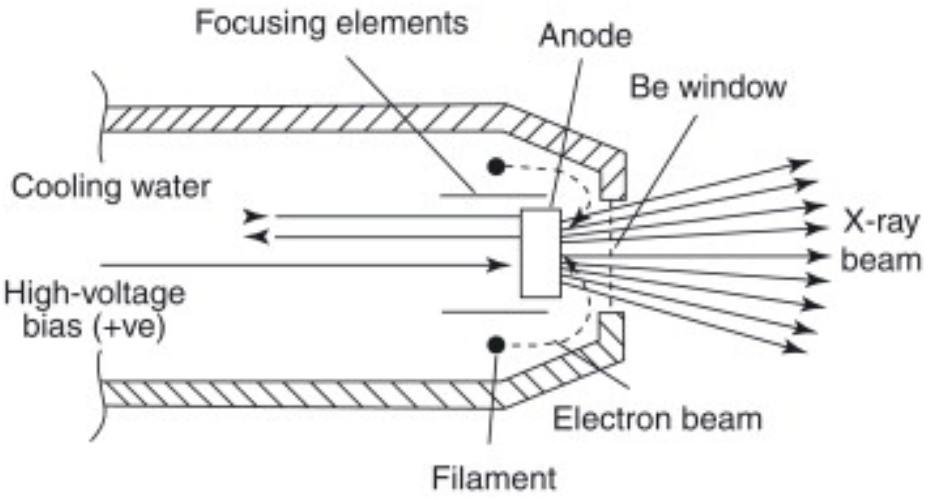

Figure 1.7: Schematic representation of X-ray tube [42]

organic hydrogen peroxide compounds, which can be achieved with Antioxidants. So Antioxidants are in usage to defend the body itself from indirect radiation interaction on cellular level and have high attention as a cancer prevention agent[6].

1.6 Generation of ionizing radiation

1.6.1 High energy X-rays and gamma radiation

The X-ray tube is a source of high-energy X-ray photons. High energy X-rays are generated by bremsstrahlung if energetic electrons strike a material. As mentioned in section 1.3 this type of radiation is emitted by energetic electrons if a deflection by a strong electric field near an atomic nucleus happens. The energy of incident electrons and the atomic number of the target material increases the efficiency for converting electron beam power to X-ray power. The target material, where the electrons strike, must be metallic that it withstands the impingement of a high power electron beam. The most practical target materials are tungsten, tantalum and gold, because of their high melting temperatures and high atomic numbers. To achieve a maximum X-ray emission in forward direction of the electron beam the optimum target thickness must be about 40% of the electron range. If the target thickness is greater than the optimum then the forward direction decreases but X-ray absorption increases and electron scattering within the target happens. The target is usually cooled with a flowing water stream, this is done to absorb the incident electron within the target, which would cause a high dose in a thin layer at the surface of the irradiated target material. A schematic representation of X-ray tube is shown in figure 1.7 [42]. The conversion efficiency from incident electron

beam power to emitted X-ray power in forward direction is about 8 to 9% at 5 MeV, 12 to 13% at 7.5 MeV and 16 to 17% at 10 MeV, for a tantalum target with optimum thickness. Also the angular distribution effects the penetration of the X-rays. Therefore a narrow angular distribution of Bremsstrahlung leads to an increment of the penetration in material. This happens because most of the intense zone of the emitted radiation is perpendicular to surface of the irradiated products. The advantages of the narrow angular distribution are a change in product density and dose requirements in irradiation facilities, because the X-rays mainly irradiate the product carrier which is in front of the target. The product carrier, which is adjacent, get smaller doses before and after it passes the X-ray beam [9].

1.6.2 High energy particle radiation

The production of high energy particle radiation with an accelerator demands that particle beams are delivered with sufficient energy for the required nuclear reactions and they must have sufficient beam current to get good yields.

Linear energy accelerators (LINACs)

The operation principle of a linear energy accelerator is based on the fact that a charged particle changes its energy if it is acted on by an electric field. The energy change is achieved by applying alternating potentials in a proper sequence so that the particle remains accelerated. This behaviour is practically achieved by using hollow electrodes, which are so called drift tubes. The particle is drifting at a constant velocity within the drift tube and is accelerated between the drift tubes. Therefore positively charged particles are pulled in the drift tube and afterwards pushed out of the tube due to a phase change of the accelerated field. This principle is shown in figure 1.8[2].

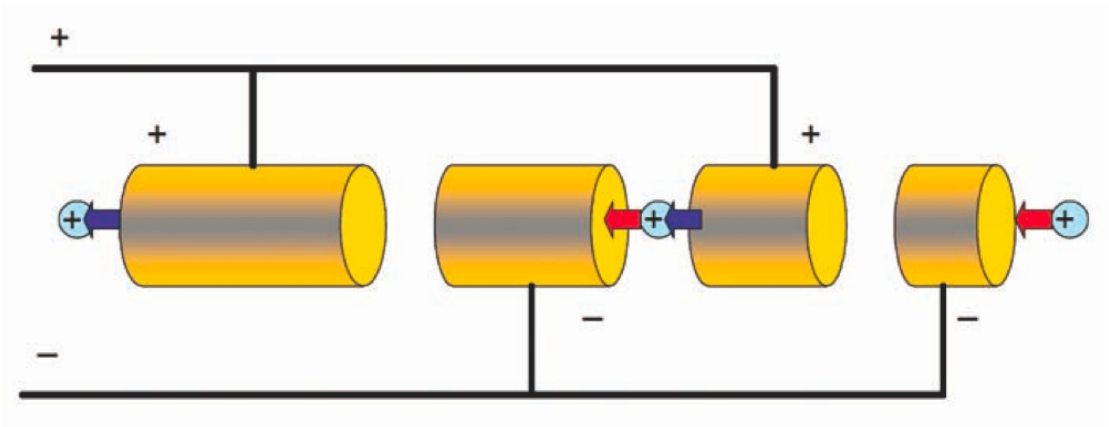

Figure 1.8: Operation principle of a LINAC[2]

Cyclotrons

The operation principle of Cyclotrons is based on the theory of electrodynamics, so the rotational frequency of a charged particle, which travels in a magnetic field, is independent of the orbit radius as long as the particles are non-relativistic. If the velocity of the particle increases the particle energy increases. Therefore the cyclotron produces high energy particles in a relatively small space. Figure 1.9 shows that the acceleration chamber of the cyclotron is located between the poles of the homogeneous magnetic field, which causes particles to travel in circular orbits. Initially, ions are generated in the centre of the machine and accelerated out from the centre. High frequency electric fields are accelerating the ions by use of so called dees, which are some hollow electrodes. Acceleration of the ion is happening if the ion passes from one dee to the next through a gap between the dees. The energy of the particles increases, because the rotational frequency of the particles is constant and diameter of the orbit increases until the high energy particle is extracted from the machine[2].

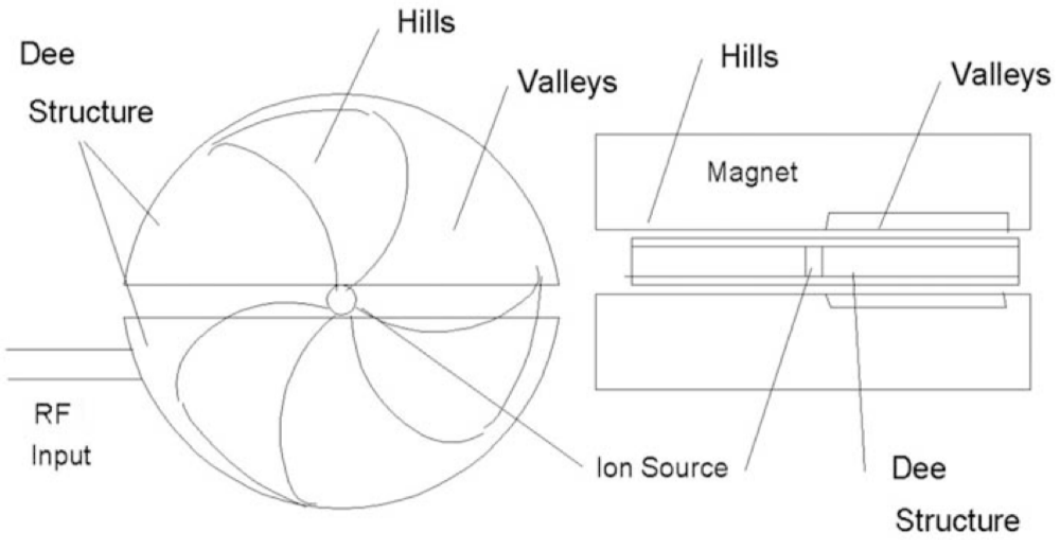

Figure 1.9: Structure of a cyclotron[2]

Synchrotron

A synchrotron represents a circular particle accelerator, which is able to accelerate ions or charged fundamental particles to high velocities close to relativistic velocities. A synchronised high- frequency alternating electrical field is used for acceleration. A magnetic field of electromagnets is readjusted depending on the achieved energy of the particles to keep the particles on a closed track. The particle trajectory lies in ultra high vacuum to avoid any energy loss due to particle collision with gas particles[37].

1.6.3 Beam delivery systems in proton and light ion therapy

Two main techniques of beam delivery systems in proton and light ion therapy are used:

- Passive scattering technique
- Active scanning technique

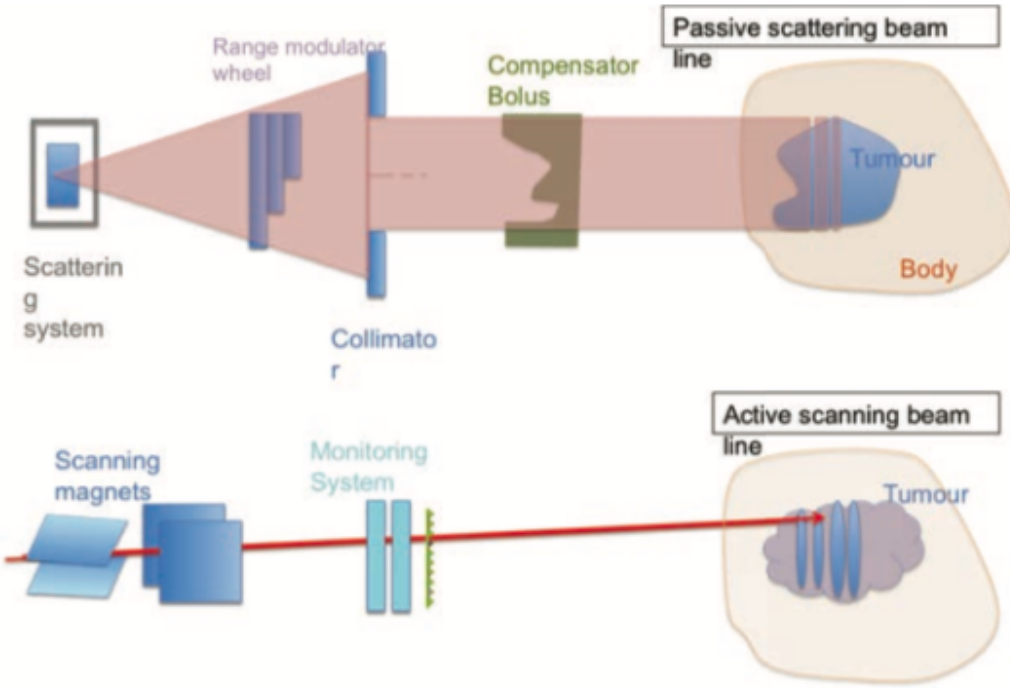

Figure 1.10: Passive scattering and active scanning beam delivery system [12]

Figure 1.10 shows the two different beam delivery systems. The passive scattering technique is based on the fact that the beam is spread by use of scattering material which is placed into the path of the particle. Collimators and compensators are conforming the dose to the target volume and ridge filters or a set of range modulator wheels are placed in the beam path to spread out the Bragg peak.
In the active scanning technique, the ion beams are deflected and steered by magnets. A single mono- energetic beam is steered by a scanning magnet to paint the target volume voxel by voxel. This is done in successive layers and the penetration depth of the Bragg peak is varied by adjusting the initial kinetic energy of the beam [12].

1.6.4 MedAustron

The MedAustron Ion Therapy Center in Wiener Neustadt delivers protons and carbon ions. A linear accelerator pre-accelerates the charged particles on a straight path by

alternating electrical fields, which continues with an injection into the synchrotron. The synchrotron is a circular accelerator and its diameter is about 30 meters. It accelerates the particles further until they reach their final velocity. Finally, the ions enters the extraction beam lines in the irradiation rooms. The particles are all the time within a vacuum tube until they left the nozzle and they are focused by strong magnetic fields, which is generated by 300 magnets[36].

1.7 Dosimetry

Radiation dosimetry deals with the measurement of dosimetric quantities, which results from the interaction of ionizing radiation with matter. In particular it is related to the determination of radiation quantities like for example exposure, Kerma, absorbed dose fluence and dose equivalent. Any device that is capable of providing a measure of the absorbed dose D deposited in its sensitive volume V by ionizing radiation is called dosemeter [4].

1.7.1 Ionization chamber

In radiotherapy the ionization chamber is the most used type of dosimeter in the clinic. The ionization chamber is available in a huge variety of designs for different usages[4]. In order to achieve clinically relevance accuracy or measuring and determining absorbed dose, various correction factors are required to be applied to the read out of the ionization chamber to correct the reading in actual circumstances to reference conditions. Some of the correction factors are listed below:

- Temperature and pressure correction factor ktp
- Beam quality correction factor kq
- Polarity effect correction factor $kpol$
- ion recombination factor ks

The correction factor ktp represents a temperature and pressure correction due to deviation from reference temperature and pressure (Details see 7.1).
Another correction factor is the kq, which represents a correction for the difference in chamber response between the reference and clinical beam quality (reference beam quality is usually 60Co) [27].
The correction factor $kpol$ considers a correction of the polarity effect to correct for the different response between negative and positive polarity. The other one is the recombination factor ks, which considers a correction of the incomplete collection of the charge, which is induced in the ionization chamber due to ion recombination in the gas cavity of the chamber [34].

The absorbed dose to water $D_{w,Q}$ is achieved by applying all correction factors:

$$D_w, Q = M_Q N_{D,w,Q_0} k_{Q,Q_0} \prod k_i \tag{1.4}$$

M_Q represents the electrometer reading, N_{D,w,Q_0} is defined as the calibration factor in terms of absorbed dose to water in reference beam and k_i are all applied correction factors.

Polarity effect

The polarity effect of the ionization chamber happens mostly due to capture by the ionization chamber collection electrode of an amount of the primary electrons. Some additional charge, which depends on the polarity of the supply voltage of the chamber, may be added or subtracted from the true ionization channel, if this captured electrons are not balanced by ejection of recoil electrons from the collecting electrode [34].
The mean of the readings at negative and positive polarizing voltages should be taken as the corrected reading, if the readings with opposite voltages differ from each other:

$$M_{true} = \frac{\mid M_+ \mid + \mid M_- \mid}{2} \tag{1.5}$$

M_{true} represents the corrected reading, $\mid M_+ \mid$ is the reading, which is obtained with positive polarizing voltages, and $\mid M_- \mid$ is the reading obtained with negative voltages. The polarity correction k_{pol} is of the reading is calculated in the following way [3][26]:

$$k_{pol} = \frac{\mid M_+ \mid + \mid M_- \mid}{2 \mid M_- \mid} \tag{1.6}$$

Recombination effect

Two types of ion recombination mechanism can be distinguished: initial recombination and volume recombination. The ion recombination effect is dependent on different parameters, like particle type, linear energy transfer, beam quality, beam delivery method, operating voltage, dose rate, and chamber geometry[47].

The initial recombination is created between ions in the same ionisation track and is independent of the ionisation current but is related to the ionisation density within the track. Therefore it has an higher impact to the total ion recombination in high linear energy transfer beams than in low linear energy transfer beams. The theories of Jaffé and Kara- Michailova are describing the initial recombination [47][18].

The volume recombination takes place between ions, which are originated from different ionisation tracks and therefore it is related to the dose rate in continuous beams or dose per pulse in case of pulsed beams. The theory of Boag is describing the volume

recombination in the near saturation regime for different structures of the beam current [47][5].

Initial recombination:Jaffé's model
The model of Jaffé is assuming that the density has a Gaussian spatial distribution which is perpendicular to the track starting with an initial mean-square radius b and widening with increasing time diffusion [47][18].It is assumed that the ionisation density is constant along the section of the track crossing the ionisation chamber [5].

Volume recombination: Boag's models
Boag has shown with his model that for continuous beams, the inverse of the current varies linearly with the inverse square of the polarizing voltage. For pulsed beams, the inverse of the current varies, to first order, linearly with the inverse of the polarizing voltage [5]. For pulsed beams,the length of the pulse (T_2) should be short compared to the ion collection time (τ_c). Moreover, the collection time (τ_c) should be much shorter as the time between the pulses (T_1):

$$T_2 << \tau_c << T_1 \tag{1.7}$$

Figure1.11 shows the representation of schematic time structure of a continuous beam produced by a synchrotron.

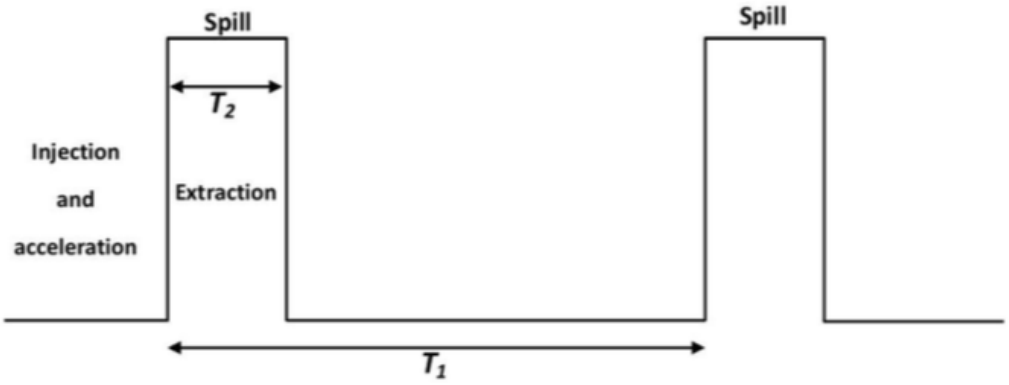

Figure 1.11: Representation of schematic time structure of a continuous beam produced by a synchrotron. [47]

Calculation of recombination effect
The recombination effect can be calculated approximately by calculating the ratio of the saturation current and current at operating voltage V for continuous beams in the following way[32]:

$$\frac{I_{sat}}{I_V} = 1 + \frac{A}{V} + \frac{m^2 * g}{V^2} * I_{sat} \tag{1.8}$$

I_{sat} is the saturation current, I_V is the operating voltage current, parameter m^2 represents the volume recombination parameter, which depends on the recombination coefficient and the mobility of positive and negative ions in the gas of the ionization chamber. A is a constant dependent on the chamber type and g is dependent on the chamber geometry, g defined as $d4/6v$, with d as the plate separation and v as the collecting volume of the chamber.

If a 1/n fraction of a polarizing voltage V is calculated, where n is larger than unity equation 1.8 becomes:

$$\frac{I_{sat}}{I_{V/n}} = 1 + n * \frac{A}{V} + n^2 * \frac{m^2 * g}{V^2} * I_{sat} \tag{1.9}$$

If the equation 1.9 is divided by equation1.8, higher terms are neglected and I_{sat} is approximated by I_V, it results to following approximation:

$$\frac{I_V}{I_{V/n}} \approx 1 + (n-1) * \frac{A}{V} + (n^2-1) * \frac{m^2 * g}{V^2} * I_V \tag{1.10}$$

The second term on the right side of the equation 1.10 represents the initial recombination and the third term is related to the volume recombination [24][47].

Chamber response heterogeneity

Previous studies ([40], [41], [29]) investigated the response uniformity of Large area ionisation chambers (LAICs) of a different vendor (ie. PTW, Freiburg Germany). The dose area product measurements are representing an alternative to central-axis point dose measurements. Using such detectors requires detailed information on the uniformity of the response along the sensitive area [40].
For scanned beams it is practical to calibrate the beam monitor by use of number of particles in a single beamlet or its dosimetric equivalent, which is the dose area product in water (DAPw).The DAPw is obtained by use of the Hartmann-method in a single - layer scanned field via measurement of dose to water. It is also proposed to determine DAPw by use of large-area plane-parallel ionization chambers. These chambers are directly integrating the dose over an area, which is perpendicular to the beam axis.
The correction factor k_{NU} is used for the calculation of DAPw and is proposed to counteract the heterogeneous response during absolute dosimetry measurements. The correction factor k_{NU} is calculated individually for each chamber based on the equation 1.11.

$$k_{NU} = \frac{\int\int_A D_{w_{Q_{spot}}}(x,y)dxdy}{\int\int_A r(x,y)D_{w_{Q_{spot}}}(x,y)dxdy} \tag{1.11}$$

$D_{w_{Q_{spot}}}(x,y)$ represents the 2D lateral absorbed dose to water profile and $r(x,y)$ is defined as the relative response as a function of lateral offset, which can be expressed

normalized to the average response over the entire area (A). The relative response $r(x, y)$ is calculated with equation 1.12. $R(x, y)$ is defined as the detector response to a theoretical, dimensionless pencil beam of non scattering particles at lateral position (x,y) with respect to the chamber's center [40].

$$r(x, y) = \frac{AR(x, y)}{\int\int_A R(x, y)dxdy} \tag{1.12}$$

CHAPTER 2

Materials

2.1 X-ray unit

The X-ray unit is an YXLON Maxishot (YXLON International GmbH, Hamburg, Germany), which is oil cooled and commercially available (shown in figure 2.1)[20]. The X-ray tube (type Comet Y.TU/320-D03) is mounted at the side of the steel container to provide a horizontal beam. The container's dimensions are 1299 x 928 x 1384 mm. Target material of the X-ray unit is tungsten and the angle is 20°. The accelerating voltage can be varied between 10 and 200 kV and the maximal current is 21 mA. The focus size can be switched between 3.0 mm and 5.5 mm. The prefiltration consists of 3.0 mm Be, 3.0 mm Al and 0.5 mm Cu. The half value layer at this filtration is 13.2 mm Al at 200 kV [20][49].

Figure 2.1: Yxlon X-ray unit

The acceleration voltage, the current, the focus size as well as the irradiation time are adjustable via an outside control unit[39][23].

2.2 Water phantom

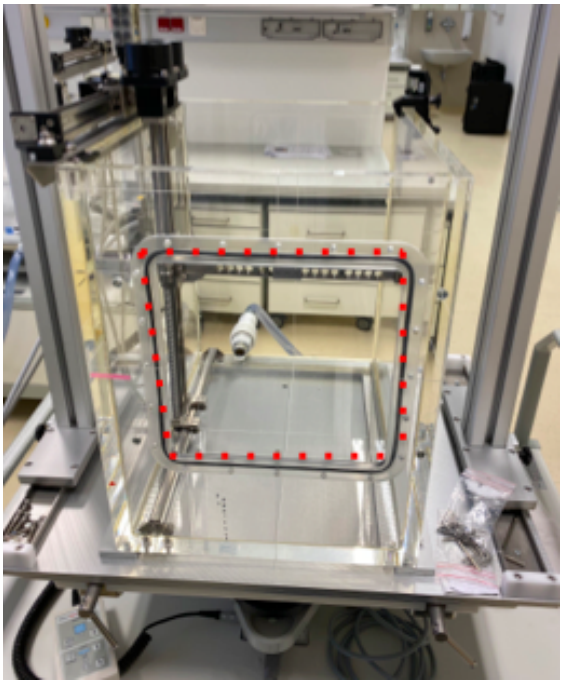

Figure 2.2: MP3-P:the red dots mark the entrance window of the MP3-P phantom

The MP3-P and MP3-PL Phantom from PTW (PTW Freiburg GmbH, Freiburg, Germany) [15][16] were used during this measurements. They are especially designed for dosimetry in photon and particle beams. The MP3-P, which was the smaller water phantom, was used in YXLON unit during photon measurements, because the MP3-PL did not fit into the YXLON. The larger MP3-PL water tank was used during measurements with protons and carbons ions. Details of the most important technical specifications for the two water phantoms are listed in Table 2.1. The water phantom consisted of a moving mechanism with a control unit and a PMMA tank. The movement mechanism consisted of three arms labeled A, B and C and which can be moved along the lateral, longitudinal and vertical axis with a step interval of 0.1 mm and positioning accuracy of 0.5 mm. The position was adjusted directly via a control pendant or remotely by a TBA CONTROL UNIT (PTW Freiburg GmbH, Freiburg, Germany) and the software MEPHYSTO (Medical physics tool, PTW, Freiburg GmbH, Freiburg, Germany). The entrance window of the water tank was thinner than the rest of the water phantom and can be removed. The measurements with photons were executed without any entrance

	MP3-P	MP3-PL
Outside dimensions [mm]	484 x 498 x 386	630 x 520.5 x 632
Moving range [mm]	350 x 380 x 250	500 x 408.5 x 500
Wall thickness [mm]	18	18
Entrance window dimensions [mm]	250 x 250 x 0.5	250x250 x 0.5
WET of entrance window [mm]	5.84 ± 0.01	5.85 ± 0.01
Filling capacity [l]	72	170
Step interval [mm]	0.1	0.1
Position accuracy[mm]	0.5	0.5

Table 2.1: Selection of technical specifications for the MP3-P and MP3-PL water tank according to PTW manual [15][16]

window, the measurements with protons and carbon ions were done with the entrance window.

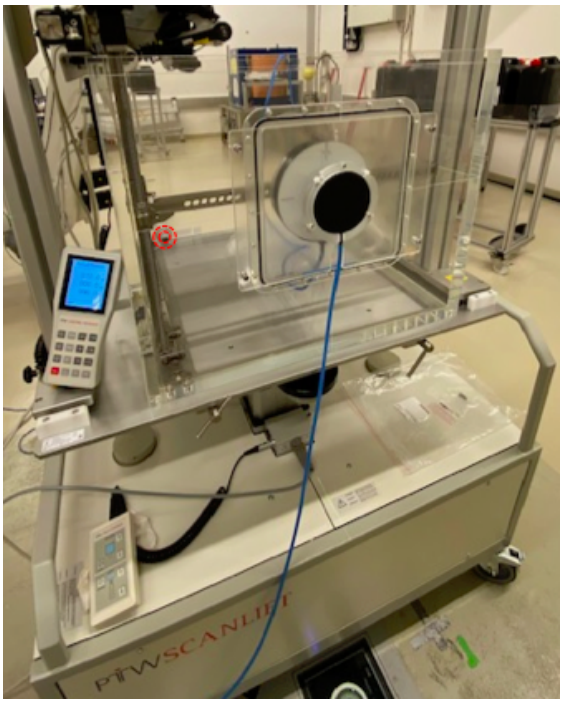

Figure 2.3: The MP3-PL water tank is mounted on a water reservoir, where the water can be directly pumped into the phantom, which is marked red

Generally the water tank was mounted on a water reservoir, so that the water can be directly pumped into the water phantom, which is marked red and shown in figure 2.3.

The water tank was dismounted from the water reservoir during measurements inside the YXLON X-ray unit and the measurements were performed in air [39][23].

2.3 Ionization chambers

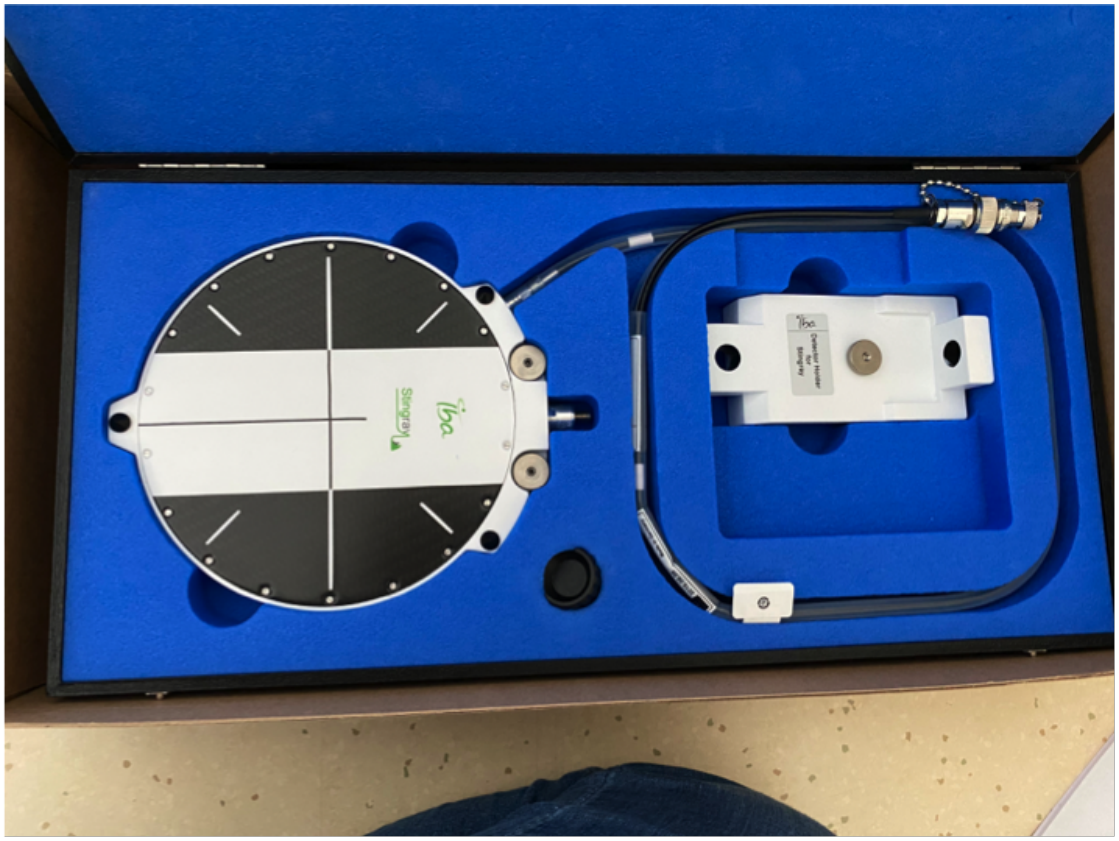

Figure 2.4: IBA StingRay chamber with holder

Two IBA StingRay Chambers (SN91 and SN93) with a housing diameter of 156 mm from IBA (IBA Dosimetry GmbH, Schwarzenbruck, Germany)[19] were used. The manufacturer specifies a circular active diameter of 120 mm, a nominal thickness of top electrode of 1.00 mm, a nominal thickness of painted housing cover of 2.2 mm, and an air gap between housing cover and top electrode of 0.6 mm [19]. An additional serial number specific certificate with different entrance window thicknesses for each chamber is given by the vendor and attached in the appendix of this thesis. The nominal voltage is +150 V, which was used for all measurements. Figure 2.4 depicts the IBA StingRay chamber with its holder. The top collecting electrode as well as the back polarizing electrode consist of Graphite with a density of 2.2 g/cm^3, the chamber stem consists of Aluminium with a density of 2.7 g/cm^3 and the housing cover is made of carbon with a density of 1.56 g/cm^3 [19]. The IBA StingRay chamber was used in combination with a

reference chamber PTW 34080, which is a thin window Bragg Peak chamber, details of all chambers are listed in table 2.2 [39].

Ionization chamber	Serial number	WET [mm]
PTW 34080 (thin window Bragg Peak chamber)	SN42	1.95
IBA StingRay (large area Bragg Peak chamber	SN0091	5.06
IBA StingRay (large area Bragg Peak chamber	SN0093	4.94

Table 2.2: Used ionization chambers and corresponding WET [19][16][13]

2.4 Electrometers

The DOSE1 (serial number 20591) is a portable, single channel, high-precision reference class electrometer from vendor IBA (IBA Dosimetry GmbH, Schwarzenbruck, Germany)[25] which was used with the IBA StingRay chambers. It measures the dose, dose rate, average dose, charge, current and dose per monitor unit [25].

A PTW Unidos webline electrometer [14] with serial number 883 was used for the reference chambers. The measured dose and dose rate units can be given as radiological units, provided the detector had been adequately calibrated, or in the electrical units charge (C) and current (A)[39].

2.5 Particle irradiation at MedAustron

The Medaustron Ion Beam Therapy Center in Wiener Neustadt has a slow- extraction synchrotron, delivering proton and carbon ion beams [36]. The proton beam is available for nominal energies from 62.4 MeV to 252.7 MeV with ranges from 3.0 cm up to 38.0 cm in water. The maximum field size of the proton beam is 20 x 20 cm^2. The Carbon ion beam has nominal energies from 120.0 MeV per atomic mass unit to 402.8 MeV per atomic mass unit which corresponds to 2.9 cm up to 27.0 cm in water. The maximum field size of the carbon ion beam is 20 x 20 cm^2. Typically, the extraction is performed in 5 s spills and the time between spills is approximately 4 s, which is used for resetting the magnets, injecting and accelerating to particular beam energy. The beam is delivered into the treatment rooms, if the extracted beam is deflected into one of the beam lines by use of focusing magnets and two orthogonal scanning magnets. The full width at half maximum (FWHM) of the lateral profile of the open beam (without any range modulating devices) at isocentre is varying from 7 up to 22 mm for protons from the highest to lowest energies. Whereas for carbon ions, the FWHM ranges from 6 to 10 mm

for the highest to lowest energies. A so-called dose delivery system (DDS) controls the beam after the accelerator exit window. The dose delivery system consists of two sets of nitrogen fluxed parallel plate ionization chambers, where each of them is providing an integrated signal and horizontal as well as vertical signal distributions by using a strip electrode configuration. The delivery of the planned number of particles for each spot is controlled with integral monitor chambers[44]. For carbon beams two ripple filters are inserted before the exit window to broaden the Bragg peaks.

CHAPTER 3

Methods

3.1 Lateral response of IBA StingRay plan parallel ionization chamber for narrow beam photon and proton dosimetry

3.1.1 Experimental setup with X-ray beam

A schematic representation of the experimental setup can be seen in figure 3.1.

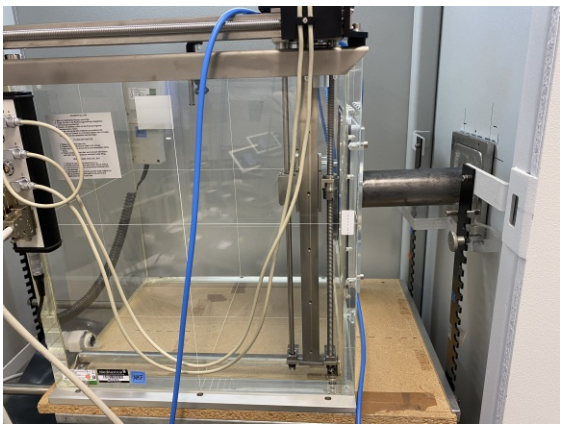

(a) Experimental setup in Yxlon

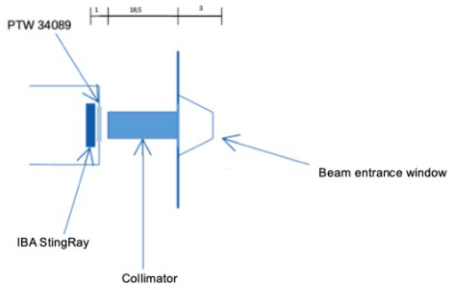

(b) Schematic representation of experimental setup in the Yxlon with certain distances of the setup given in unit [cm]

Figure 3.1: Experimental setup with X-ray beam

The MP3-P water phantom was placed inside the steel container of the Yxlon X-ray unit on a wooden plate. The entrance window of the MP3-P water phantom was located

at the same height as the beam exit window of the Yxlon X-ray unit. Therefore the distance from inside bottom to the top of the wooden plate was 41 cm. In front of the beam exit window of the Yxlon X-ray unit an in-house built collimator was attached see figure 3.1. The IBA StingRay chamber was mounted on the movement mechanism of the MP3-P water phantom and was the chamber of interest, whereas a transmission monitor chamber was mounted with a telescope holder between the IBA StingRay chamber and the in-house build collimator. The beam exit opening of the collimator was aligned with the centers of the IBA StingRay chamber and the monitor transmission chamber by use of radiochromic EBT3 films. The distance between the IBA StingRay chamber to beam entrance window was in total 23.5 cm. The IBA StingRay chamber was moved with the hand panel of the MP3-P water phantom in the different directions. The IBA StingRay chamber response was gathered with the IBA Dose 1 and the transmission chamber response with the PTW Unidos.
All measurements were done with a setting of 200 kV, 20 mA and a focal spot of 5.5 mm. The X-ray beam size produced by the collimator was measured by using radiochromic EBT3 films. The beam size was determined to obtain the dimensions of the spot which is used to approximate a Gaussian profile.

3.1.2 Experimental setup with proton beam

The response of the IBA StingRay chamber was measured with a proton beam to compare and confirm the response gathered by the investigation in photons.

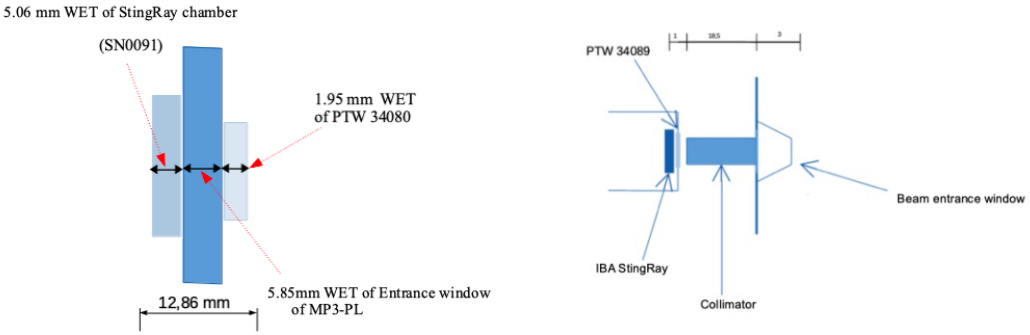

(a) Total WET for setup with proton beam

(b) Schematic representation of experimental setup with proton beam

Figure 3.2: Experimental setup with proton beam

The experimental setup is depicted in figure 3.2. The large water phantom MP3-PL was used. The IBA StingRay chamber was mounted on the mechanism of the MP3-PL and aligned at isocenter position in parallel direction to the proton beam. A transmission chamber was mounted with a telescope holder between the IBA StingRay chamber and the proton beam. Centers of the chambers were aligned with the beam center by use

of the laser guide system of IR1. The used proton beam energy was 252.7 MeV. The IBA StingRay was moved with the MEPHYSTO software and the chamber response of the IBA StingRay was gathered with the IBA Dose 1 electrometer. The response of the transmission chamber was gathered with the PTW Unidos.

3.1.3 Scan patterns

In table 3.1 it is shown, which scan patterns were delivered to the IBA StingRay chambers SN91 and SN93.

IBA StingRay Chamber Serial number	Beam source	Scan pattern
SN91	Proton beam	Horizontal and vertical profile
SN91	X-ray	Horizontal and vertical profile
SN93	X-ray	horizontal and vertical profile
SN91	X-ray	Star profile
SN93	X-ray	Star profile
SN91	X-ray	Full profile
SN93	X-ray	Full profile

Table 3.1: Overview of scan patterns which were applied to different IBA StingRay chambers SN91 and SN93

The scan pattern for horizontal and vertical profile measurements is shown in figure 3.3.

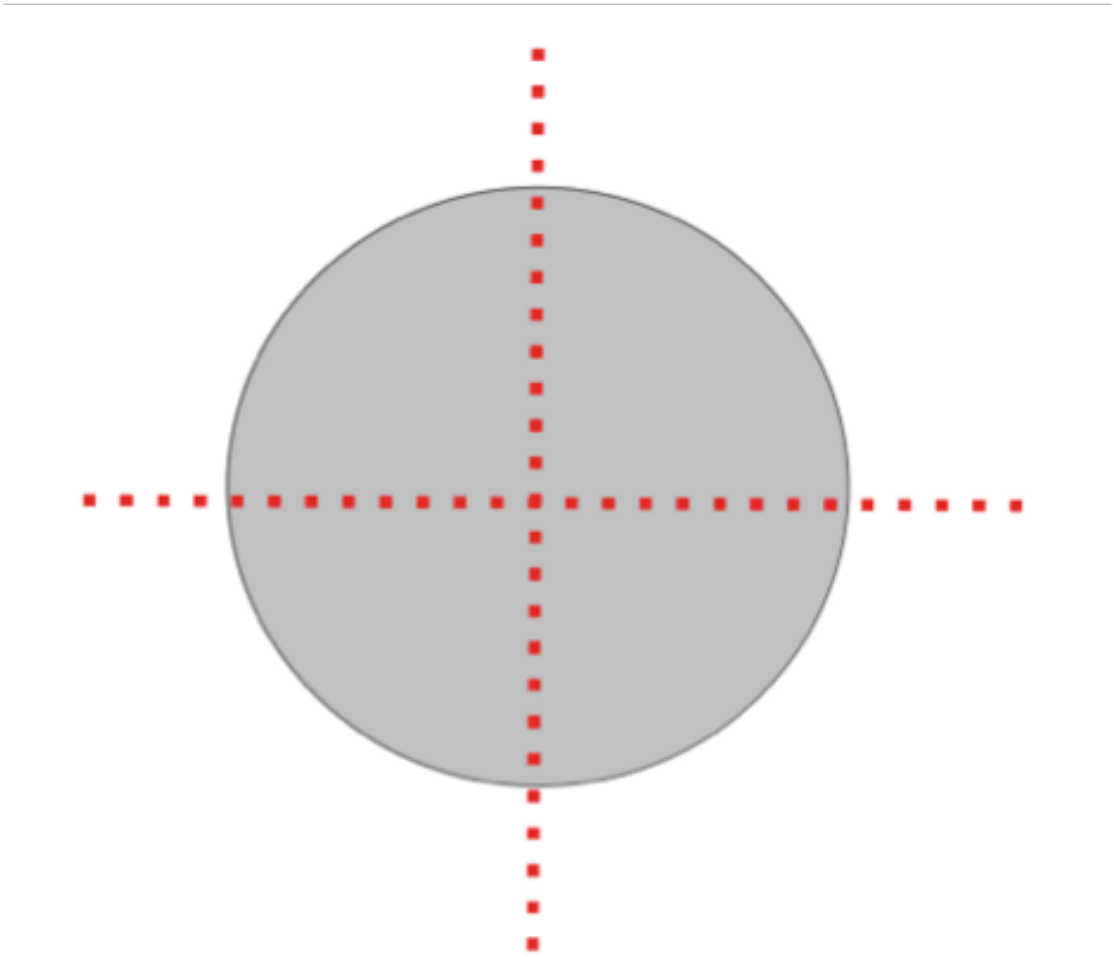

Figure 3.3: Scan pattern of horizontal and vertical profile measurement

The IBA StingRay chamber was moved perpendicular to the plain of the beam along the horizontal axis (C-Axis) with generally 5 mm steps of increment. Close to the center 2.5 mm steps of increment and close to edge 1 mm steps of increment were measured[40][41]. The IBA StingRay chamber was moved along the vertical axis (B-axis) with the same pattern like the horizontal profile to gather the vertical profile of the IBA StingRay chamber.
This horizontal and vertical profile measurement were done with IBA StingRay chamber SN91 and SN93 and were executed by use of an X-ray beam with irradiation time of 10 s for each spot and proton beam with irradiation time 0.5 s.
The scan pattern for diagonal profile measurements is shown in figure 3.4.

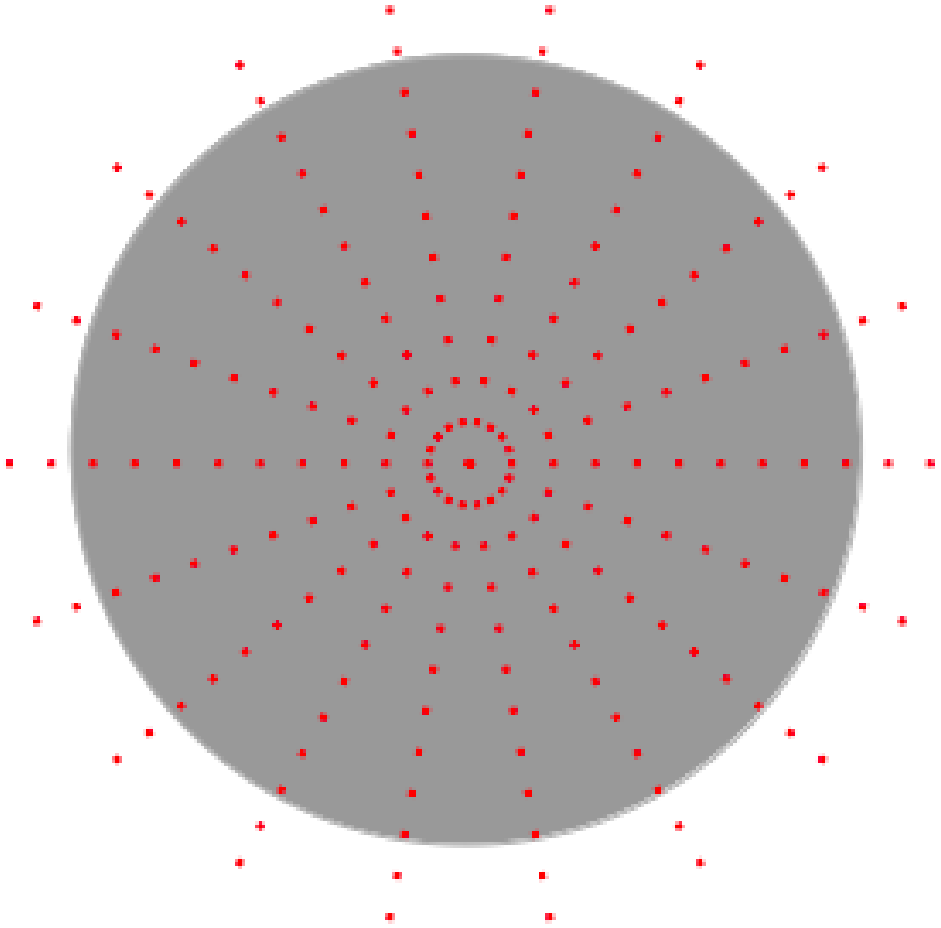

Figure 3.4: Scan pattern of diagonal profile measurement with X-ray beam

The IBA StingRay chamber was moved perpendicular to the plain of the beam along a radial pattern with 20° Degree difference [29]. So measurements for 0°, 20°, 40°, 60°, 80°, 100°, 120°, 140°, 160° and 180° were executed. This scan pattern was executed with IBA StingRay chamber SN91 and SN93 by use of an X-ray beam. The irradiation time of X-ray beam for each measurement point was 10 s.

The scan pattern for full profile measurement is shown in figure 3.5 .

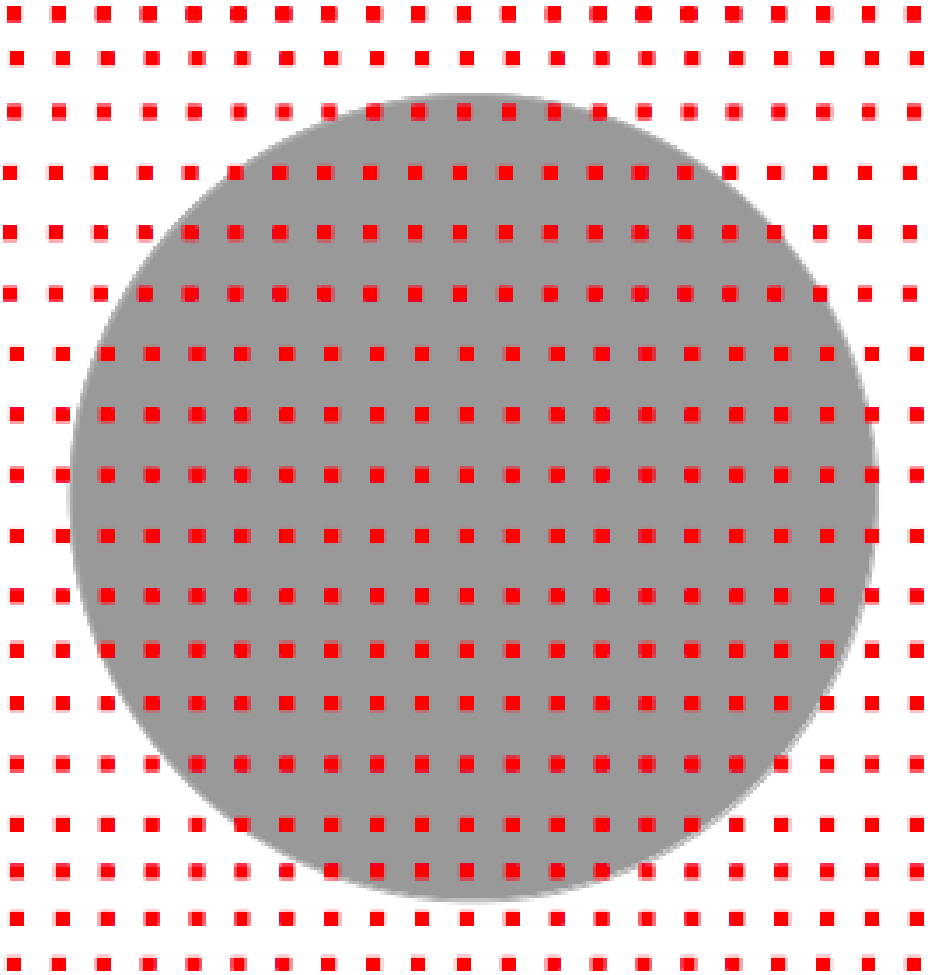

Figure 3.5: Scan pattern of full profile measurement with X-ray beam

The IBA StingRay chamber was moved perpendicular to the plain of the beam over an area of 14 cm x 14 cm in 10 mm increments [40][41]. The irradiation time of X-ray beam was 10 s for each measurement point. This scan pattern was executed with IBA StingRay chamber SN91 and SN93 by use of an X-ray beam.

3.1.4 Alignment and edge correction

Response alignment to the center of the IBA StingRay chamber

The results of the response of the IBA StingRay chamber was normalized to the center point of the chamber by applying a response-center-alignment correction on the data. Therefor the active area diameter, which is given by the vendor, is used to find the center of the IBA StingRay chamber and the following equation was used:

$$x_{new} = x + offset_x \tag{3.1}$$

$$y_{new} = y + offset_y \tag{3.2}$$

$$offset_x = \frac{x_{max+} + x_{max-}}{2} \tag{3.3}$$

$$offset_y = \frac{y_{max+} + y_{max-}}{2} \tag{3.4}$$

x_{new} and y_{new} are the center aligned coordinates. The offsets $offset_x$ and $offset_y$ are calculated by use of x_{max+}, x_{max-}, y_{max+} and x_{max-}. This are the coordinates at the edges, where the normalized chamber response is greater 80% and the total range of the profile is 120 mm, which represents the active radius of the chamber.
For the results of the IBA StingRay chamber response of the proton beam no additional alignment correction was applied because there the alignment of the chambers were done by using a laser guide system of the IR1.

Edge correction

An edge correction was applied to the chamber reading of the IBA StingRay, because the chamber response is reduced at the edge of the active area of an large area ionisation chamber. The decreased response appears because only a part of the beam hits the actual active area, which needs to be treated in a different way than an under response of the chamber. The actual part of the beam, which hits the active area, needs to be calculated for the edge correction, this is done by assuming a Gaussian beam profile for proton and photon beam with FWHM 13.33 mm for proton beam and 4.39 mm for X-ray beam, which was gathered by a radiochromic film exposed to X-ray and proton beam (see figure: 3.6).

(a) radiochromic film when exposed to a X-Ray beam. The FWHM is 4.39 mm

(b) radiochromic film when exposed to a proton beam with an energy of 252.7 MeV. The FWHM is 13.33 mm

Figure 3.6: Radiochromic films were used to gather the FWHM of the X-ray and proton beam.

The following steps were taken for the edge correction of the chamber response:
Each measurement point of the chamber response, which is outside of the active area of the IBA StingRay chamber is set to zero and every point inside of the active area radius is set to I_{corr}, which is the normalized chamber radius divided by the weight w:

$$r(x,y) = \sqrt{x^2 + y^2} \tag{3.5}$$

$r(x,y)$ is the calculated radius for each measurement point

$$F = \exp -(\frac{(x^2 - 2xr(x,y) + r(x,y)^2)}{2(\frac{FWHM}{(2*\sqrt{2*log(2)})})^2}) \tag{3.6}$$

F represents the Gaussian profile

$$w = \frac{\int_{-r_{active}+\Delta}^{+r_{active}+\Delta} F dr}{y_{tot}} \tag{3.7}$$

w is the integral of F over the whole active area of the chamber plus Δ (= the Margin) divided by y_{tot}. y_{tot} is the integral of initial F from - infinity to infinity
For all measurement points within the active area of the chamber I_{corr} is calculated in the following way:

$$I_{corr} = \frac{I}{w} \tag{3.8}$$

The proportion of the beam incident on the chamber is calculated and set in relation to the measured response for all measurement points which are unequal zero or one. This leads to an calculated correction factor. There reciprocal calculated correction factor is used further. The reciprocal value is used to avoid any problems with a division by zero. Finally the original measurement points are multiplied wit its reciprocal correction factor [23][41].

$$I_{norm2center} = \frac{I}{I_{center}} \tag{3.9}$$

$$Ic_{norm2center} = \frac{I_{corr}}{I_{center}} \tag{3.10}$$

The original chamber charge I is normalized to the charge of the center I_{center}. The corrected normalized response to the center $Ic_{norm2center}$ is calculated if I_{corr} is divided by I_{center}

The edge correction was only applied for measurement points with proton beam. The edge correction was not applied on measurement points with X-ray beam due to an increase of the chamber response at the edge of the chambers (Details see Chapter 5).

3.2 Polarity, dose stability, dose rate stability, voltage stability

3.2.1 Polarity effect

Negative and positive chamber voltages from -150 V up to 150 V were applied to the IBA StingRay chamber (SN91). The IBA StingRay was irradiated with a Carbon ion Beam energy of 120 MeV per amu and 346.6 MeV per amu. The responses of the negative and positive applied chamber voltage were compared to check if the response is indifferent of sign of the applied chamber voltage.

3.2.2 Dose stability

The dose stability of IBA StingRay chamber SN91 was determined by the linear relationship between the chamber charge and irradiation time. The dose stability was measured by applying a X-ray beam with following settings: 200 kV, 20 mA, and a focal spot of 5.5 mm. The irradiation time was increased in half-minute increments up to 5 min [39].

3.2.3 Chamber dose rate stability

The chamber dose rate stability of IBA StingRay chamber SN91 was determined by the linear relationship to X-ray tube current. The IBA StingRay chamber was irradiated for 30 seconds with X-ray tube settings of 200 kV, varying tube current from 2-20 mA in 2 mA steps and focal spot of 5.5 mm [39].

Beam quality dependence

The beam quality dependence of IBA StingRay chamber SN91 was determined by the quadratic relationship to X-ray tube voltage, as well as the one between chamber current and X-ray tube voltage. The data for the beam quality dependence were gathered with IBA StingRay chamber and following X-ray tube settings: 20 mA, a focal spot of 5.5 mm and an irradiation time of 30 seconds. The tube voltage was varied from 65-200 kV in 15 kV steps.
The beam quality dependence of the IBA StingRay was compared with the response of

the monitor chamber PTW 34089 [39].

3.3 Recombination effect

The measurements were done on two different measurement days (measurement series I: 29.02.2020 and measurement series II: 14.03.2020).
The recombination effect of IBA StingRay chamber SN91 were measured with a Carbon ion beam energy of 120 MeV per amu and 346.6 MeV per amu with degrader settings of 20, 50, and 100. Different chamber voltages were applied to the IBA StingRay: -150 V, -125 V, -100 V, -75 V, -50 V, -25 V, 25 V, 50 V, 75 V, 100 V, 125 V and 150 V
The measurements were done in three different depths, which are depicted in figure 3.7b:

- in the plateau region of the beam
- in the Bragg peak of the beam
- in the fall off region of the beam

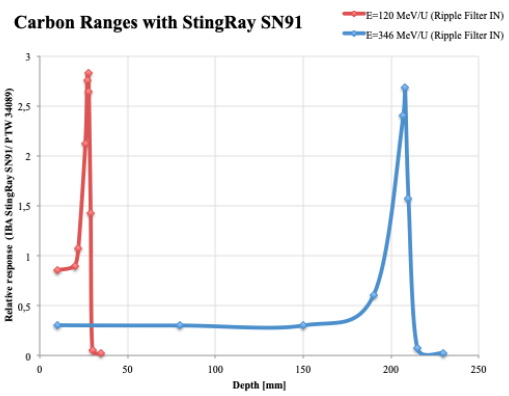

(a) IDDs of StingRay SN91 normalized to PTW 34089 for Carbon ion beam energies of 120 MeV per amu and of 346.6 MeV per amu

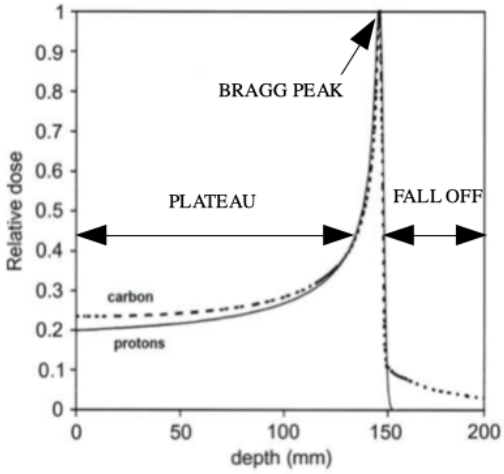

(b) The graph depicts the three different regions of the carbon ion beam

Figure 3.7a shows the Carbon ion beam ranges measured for IBA StingRay SN91 normalized to the response of PTW 34089 and for two different carbon ion beam energies. Table 3.2 shows the different depths for the different carbon ion beam energies.

Measurement series	Carbon ion beam energy [MeV per amu]	Depth of plateau [mm]	Depth of peak [mm]	Depth of fall off [mm]
I	346.6	20	208	210
I	120	18	28	29
II	120	x	27.5	29
II	120 (without Ripple Filter)	x	31	31.5
II	346.6	x	208	210

Table 3.2: Depths for different carbon ion beam energies

The measurements were also executed with different lateral offsets. Therefore lateral offsets of -30 mm, 0 mm and 30 mm were applied for carbon ion beam with energy of 346.6 MeV per amu, degrader 100 and inserted ripple filter for the peak and fall off.

CHAPTER 4

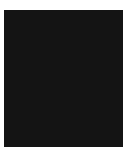

Results

4.1 Lateral response of the IBA StingRay chamber

4.1.1 Horizontal and vertical profile SN091 with X-Ray beam

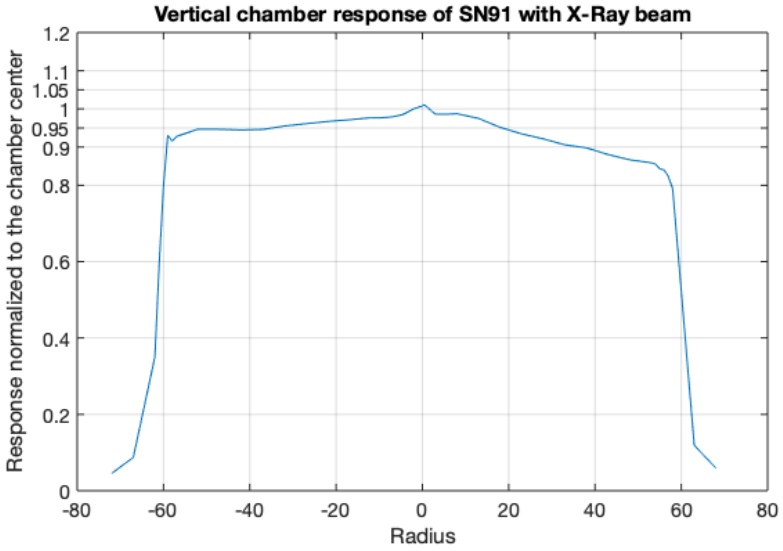

(a) Vertical response of IBA StingRay SN091 with X-ray beam

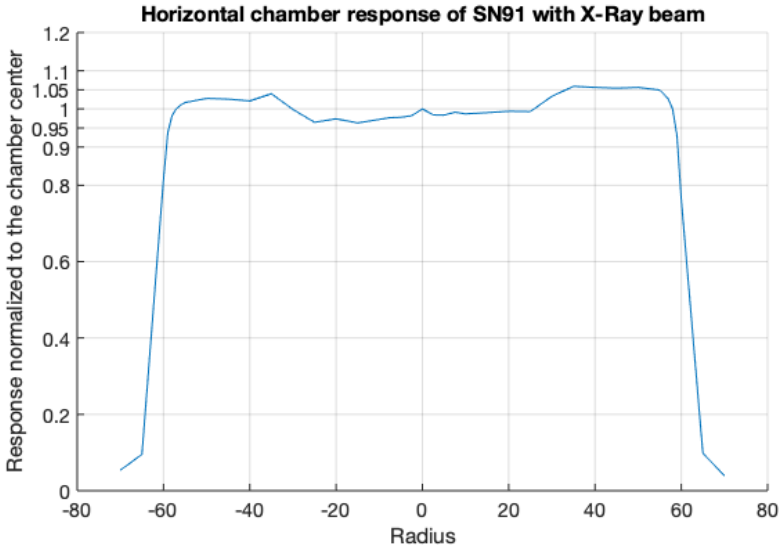

(b) Horizontal response of IBA StingRay SN091 with X-ray beam

Figure 4.1: Horizontal and vertical response of IBA StingRay SN091 with X-ray beam

Figure 4.1 shows the horizontal and vertical profile of the IBA StingRay chamber SN91 measured with X-ray beam. The number of total measurement points for each profile was 41.
The vertical profile response normalized to the chamber center has it maximum in the chamber center (= 0 mm chamber radius). From -20 mm to 20 mm it was between 95% and 100% chamber response. Then it decreased from 20 mm to 60 mm radius to 80% chamber response.The relative response normalized to the center of the chamber was higher between a chamber radius of -60 mm and 0 mm, than for the chamber radii of 0 and 60 mm.
The horizontal response normalized to the chamber center was from 0 mm to ±25 mm radius between 100 and 96%. The normalized chamber response increased at the edges from ±25 mm up to ±60 mm radius, which leads to a deviation up to +5% in comparison to the response of the center.

4.1.2 Horizontal and vertical profile SN093 with X-ray beam

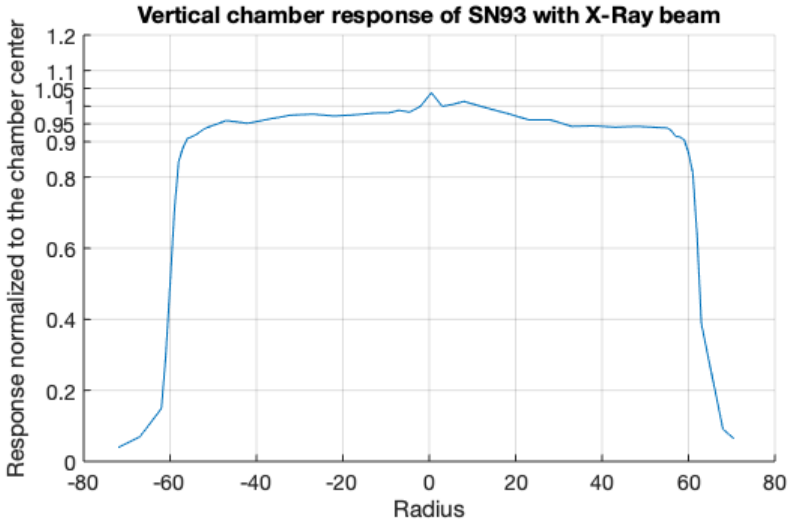

(a) Vertical response of IBA StingRay SN093 with X-ray beam

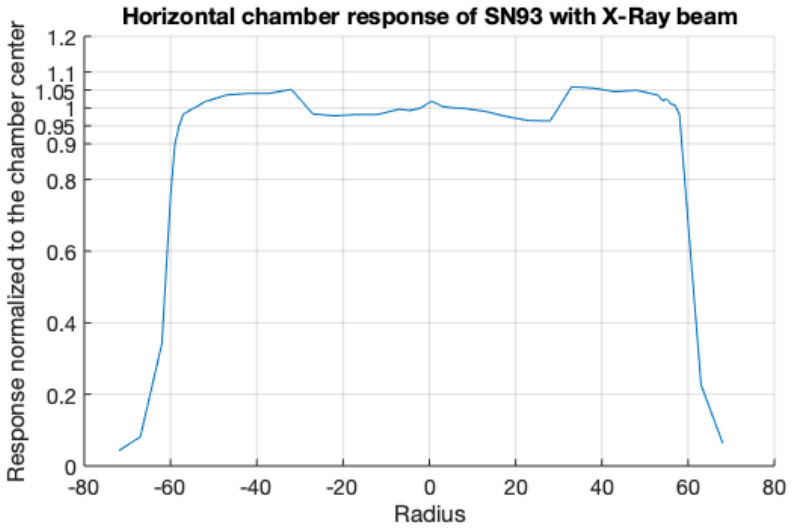

(b) Horizontal response of IBA StingRay SN093 with X-ray beam

Figure 4.2: Horizontal and vertical response of IBA StingRay SN093 with X-ray beam

Figure 4.2 shows the horizontal and vertical profile of IBA StingRay chamber SN093 with X-ray beam. The number of measurement points for each profile was 41.
The vertical response normalized to the chamber center had its maximum at the chamber center. From the center (= 0 mm radius) to ±40 mm it decreased from 100% to 95%. At the edges of the chamber, from ±40 mm to ±60 mm, it decreased further from 95% to 90%. The response of the of the lower and upper part of the chamber was overall

congruent.
The horizontal response normalized to the chamber center (was from 0 mm to ± 28 mm between 100% and 96%.From ±28 mm up to ±60 mm it increased), which leads to a deviation up to +6% in comparison to the response of the center.

4.1.3 Horizontal and vertical profile of SN91 - proton beam

Figure 4.3 shows the horizontal and vertical profile of IBA StingRay chamber SN91 measured with a proton beam. The number of total measurement points for each profile was 41. The chamber response is normalized to the chamber's center. The blue line represents the uncorrected response and the red line the edge corrected response.
The uncorrected vertical response deviation (in comparison to the center response) was between 0 and 30 mm chamber radius up to 4.7% and between 30 and 60 mm up to 19.0%. The uncorrected horizontal response deviation (in comparison to the center response) was between 0 and 30 mm chamber radius up to 2.2% and between 30 and 60 mm up to 11.7%.

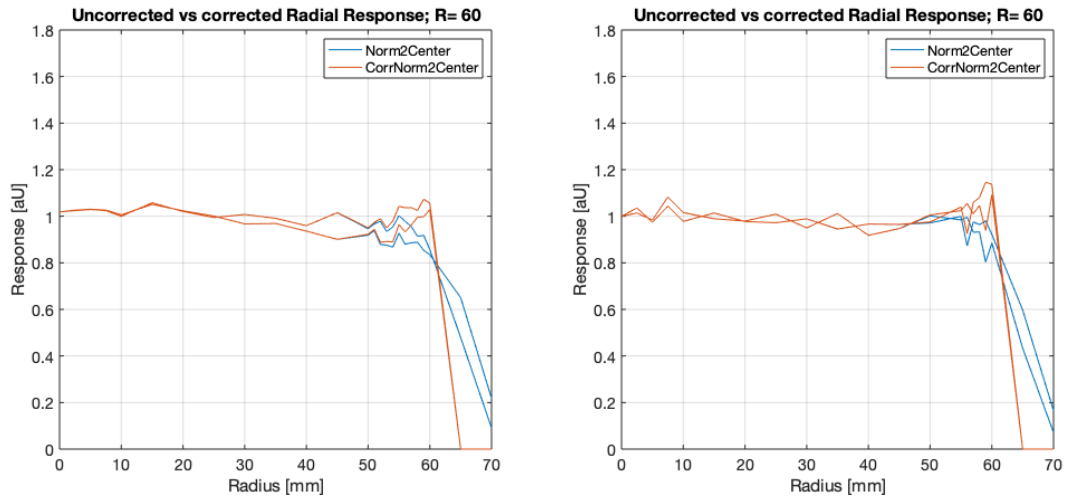

(a) Vertical response of IBA StingRay SN91 measured with a proton beam and edge correction applied with margin 0.5 cm

(b) Horizontal response of IBA StingRay SN91 measured with a proton beam and edge correction applied with margin 0.5

Figure 4.3: Horizontal and vertical response of IBA StingRay SN91 measured with a proton beam

4.1.4 Diagonal profile SN91 with X-ray beam

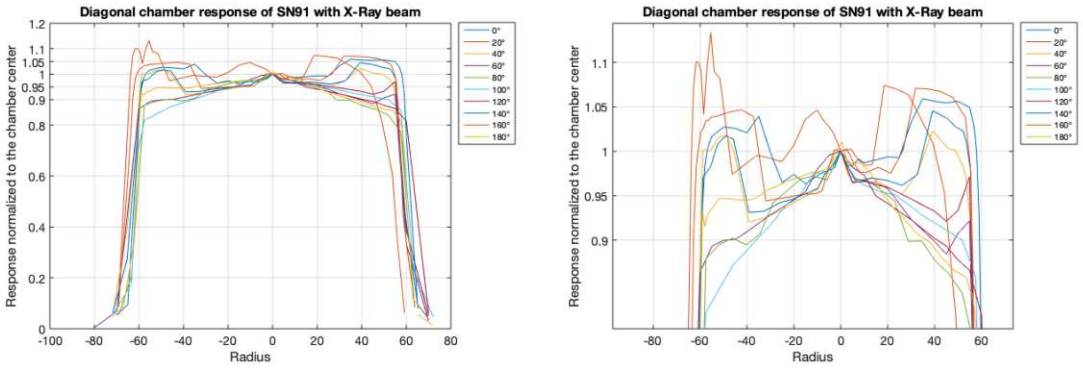

(a) Diagonal of IBA StingRay SN091 with X-ray beam

(b) zoomed diagonal response of IBA StingRay SN091 with X-ray beam

Figure 4.4: Diagonal response of IBA StingRay SN091 with X-ray beam

Figure 4.4 shows the response normalized to the chamber center of the IBA StingRay SN091, measured by diagonal profiles over the chamber. The number of measurement points was 340.
The response normalized to the center increased at the edges of the chamber from ±30 to ±60 mm) for 20°, 40°, 140° and 160°. The maximum of the response was up to +13% higher in comparison to the center.

4.1.5 Diagonal profile SN093 with X-ray beam

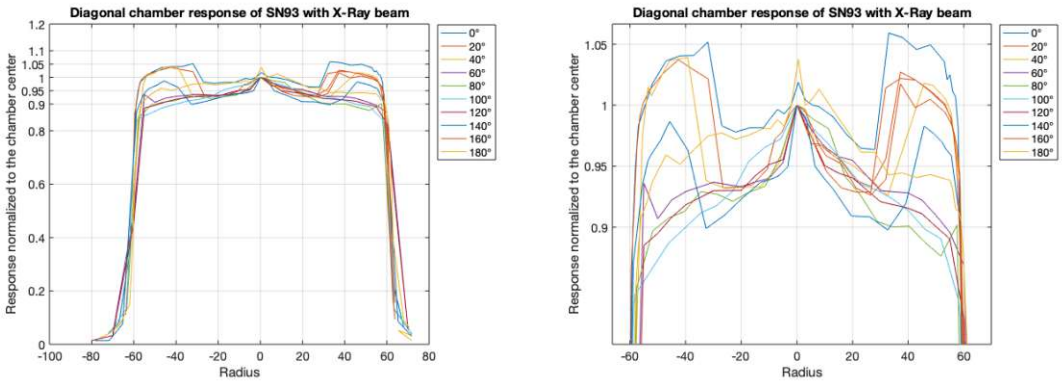

(a) Diagonal of IBA StingRay SN093 with X-ray beam

(b) zoomed diagonal response of IBA StingRay SN093 with X-ray beam

Figure 4.5: Diagonal response of IBA StingRay SN093 with X-ray beam

Figure 4.5 shows the diagonal response normalized to the chamber center of the IBA StingRay SN093. The number of measurement points was 340.
The response normalized to the center increased at the edges of the chamber (from ±30 to ±60 mm) for 20°, 40°, 140° and 160°. The maximum of the response was up to +6% higher in comparison to the center.

4.1.6 Full profile with X-ray beam

Figure 4.6 shows a dose response map of IBA StingRay SN91 and SN93 measured with X-ray beam. The different colours are representing the chamber response normalized to the chamber's center.The number of measurement points of the full profile was 323 for each chamber.

Figure 4.6a shows that the response of the IBA StingRay SN91 increased along the middle of the chamber and at the left and right side. In the upper and lower part of the chamber was no increase of the response and the upper part of the chamber had a smaller response than the lower part. The right side of the chamber had overall a more uniform response result than the left side.

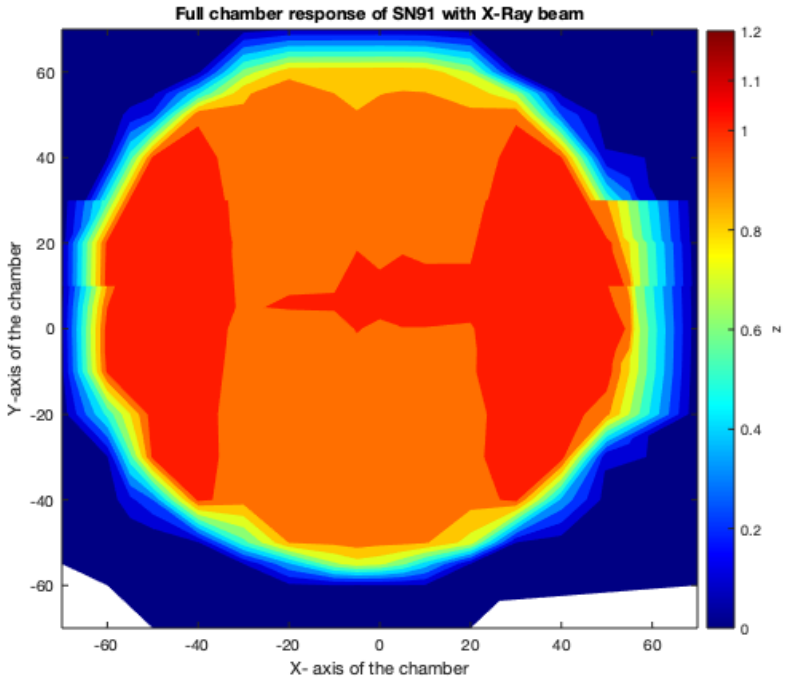

(a) Full profile response of IBA StingRay SN91 with X-ray beam. The color bar represents the response normalized to the center

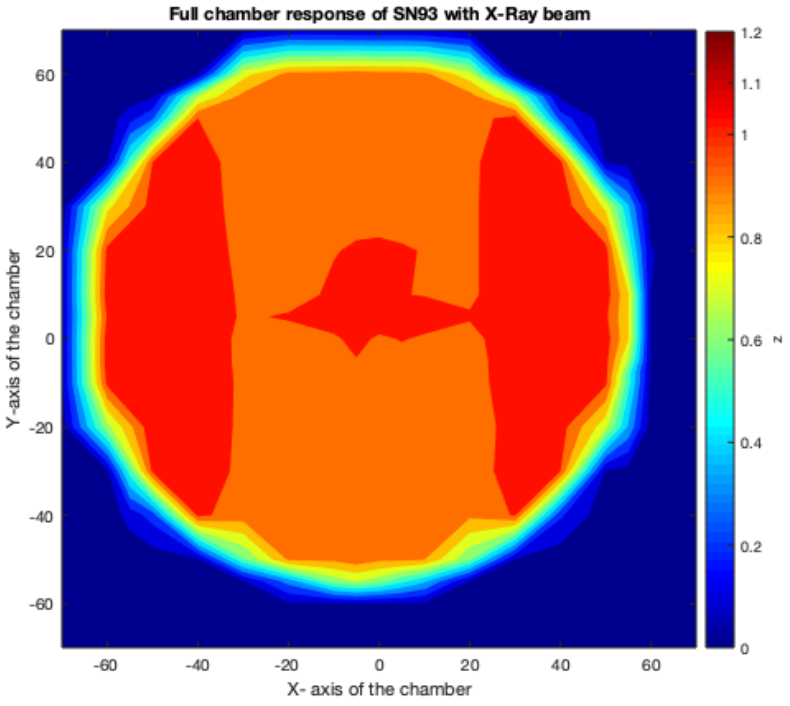

(b) Full profile response of IBA StingRay SN93 with X-ray beam. The color bar represents the response normalized to the center

Figure 4.6: Full profile response map with X-ray beam

Figure 4.6b shows a dose response map of IBA StingRay SN93 measured with X-ray beam.
The response of the IBA StingRay SN93 increased in the center of the chamber and at the left and right edges. In the upper and lower part of the chamber was no increase of the response.

The chamber response of IBA StingRay SN93 and SN91 yielded to very similar dose response maps. Except for a decrease of the chamber response of IBA StingRay SN91 at the vertical axis at 50 mm chamber radius, this decrease was not present at the response of IBA StingRay SN93.

4.2 Polarity effect, dose stability, dose rate stability

The following results are a summary of the results of measurements, which were executed in the course of a project thesis [39].

4.2.1 Polarity effect

The table 4.1 shows the result for the polarity factor k_{pol}:

Ionization chamber voltage [V]	IBA StingRay charge M [nC]	corrected IBA StingRay charge [nC]	k_{pol}
-150	56.88	58.26	1.0121
-125	56.99	58.37	1.0068
-100	56.9	58.28	1.0111
-75	58.00	59.41	0.9936
-50	56.48	57.85	1.0057
-25	54.74	56.07	0.9993
25	-54.66	-55.98	0.9993
50	-57.12	-58.50	1.0057
75	-57.26	-58.65	0.9936
100	-58.16	-59.57	1.0111
125	-57.76	-59.16	1.0068
150	-58.26	-59.67	1.0121

Table 4.1: Results of polarity effect for different applied chamber voltages from -150 V to 150 V with carbon ion beam energy 120 Mev per amu, inserted ripple filter and in the Bragg peak ion beam. The chamber charge was corrected for temperature and pressure, therefore the correction factor k_{TP}= 1.0242 was considered.

The polarity effect was tested with a carbon ion beam with energy of 120 MeV per amu in the Bragg peak of the beam, with inserted ripple filter and degrader 20. The polarity

factor k_{pol} was calculated based on equation 1.7.1. The maximum value for k_{pol} is 1.0121 for ±150 V Ionization chamber voltage, this means that the deviation between positive and negative voltage of 150 V is 1.21%. The minimum value for k_{pol} is 0.9936 for ±75 V Ionization chamber voltage, so the deviation between positive and positive voltage of 75 V is 0.64%.

4.2.2 Dose stability

The results for the dose stability of the IBA StingRay chamber measurements are shown in table 4.2 and figure 4.7.
A linear regression model was fitted to the measurement points, which is represented by the dashed red line in figure 4.7, follows:
$y = -0.0087x + 0.9027$
$R^2 = 0.23788$

Irradiation Time [min]	IBA StingRay charge M [nC]	corrected IBA StingRay charge [nC]	normalized chamber Response
0.5	18.21	19.12	1.00
1	14.97	15.72	0.82
1.5	15.76	16.55	0.87
2	14.73	15.47	0.81
2.5	15.69	16.48	0.86
3	15.36	16.13	0.84
3.5	15.32	16.09	0.84
4	15.09	15.84	0.83
4.5	15.35	16.12	0.84
5	15.22	15.98	0.84

Table 4.2: Results of dose stability for increasing irradiation time with X-ray beam. The chamber charge was corrected for temperature and pressure the correction factor k_{TP}= 1.05 was considered.

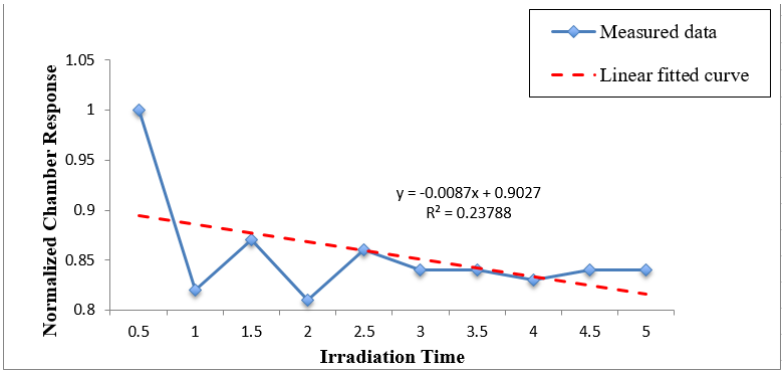

Figure 4.7: Plot for dose stability with normalized chamber response of IBA StingRay SN91 and linear fitted curve

4.2.3 Dose rate stability

Table 4.3 and figure 4.8 show the result for the dose rate stability measurements for IBA StingRay chamber SN91.
A linear fit was applied on the measurement points and shown by the dashed red lines in figure 4.8, which follows:
$y = 0.9331x - 0.384$
$R^2 = 0.099966$

X-ray tube current [mA]	IBA StingRay charge M [nC]	corrected IBA StingRay charge [nC]
2	1.48	1.56
4	3.26	3.43
6	4.86	5.11
8	6.63	6.98
10	8.49	8.93
12	10.23	10.76
14	12.22	12.86
16	13.74	14.46
18	15.52	16.32
20	17.48	18.39

Table 4.3: Results of dose rate stability for increasing X-ray tube current. The chamber charge is corrected for temperature and pressure, the correction factor k_{TP} is equal to 1.05.

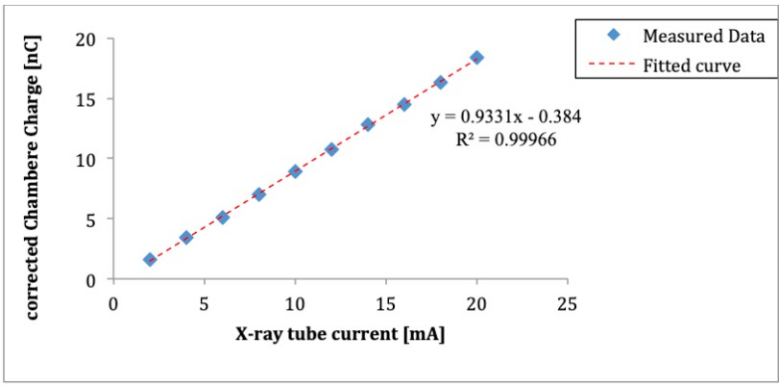

Figure 4.8: Plot for dose rate stability with X-ray beam and dashed red lined linear fitted curve: On the x-axis is the X-ray tube current and on the y-axis the corrected IBA StingRay SN91 chamber charge.

4.2.4 Beam quality dependence

The results for the beam quality dependence of the IBA StingRay chamber are shown in table 4.4 and figure 4.9.
In figure 4.9a and 4.9b a quadratic function was fitted to the measurement points, which is represented by the dashed red line in figures 4.9.
In figure 4.9c the normalized average reading at 200 kV of IBA StingRay was plotted in comparison to the PTW 34089. The blue crosses represented the normalized reading of the IBA StingRay and the red crosses the PTW 34089.

X-Ray tube voltage [kV]	IBA StingRay Charge [nC]	corrected IBA StingRay charge [nC]	Normalized Reading IBA StingRay	PTW 34089 Charge [nC]	k_{TP} PTW 34089	PTW 34089 corrected Charge [nC]	Normalized Reading PTW 34089
65	0.28	0.3	0.02	93	1.06	98.95	0.02
80	0.82	0.86	0.05	24	1.06	258.55	0.05
95	1.68	1.76	0.10	485	1.07	516.53	0.11
110	2.88	3.03	0.17	813	1.07	865.85	0.18
125	4.46	4.69	0.26	1223	1.07	1302.50	0.27
140	6.38	6.71	0.37	1713	1.07	1824.35	0.38
155	8.69	9.14	0.50	2305	1.07	2454.83	0.52
170	11.30	11.88	0.65	2963	1.07	3155.60	0.66
185	14.22	14.95	0.81	3669	1.07	3907.49	0.82
200	17.46	18.36	1.00	4480	1.07	4771.20	1.00

Table 4.4: Results of nominal tube voltage dependence for IBA StingRay SN91 and PTW 34089. The temperature and pressure correction factor k_{TP} of the IBA StingRay is 1.05 for all measurement points of the IBA StingRay SN91.

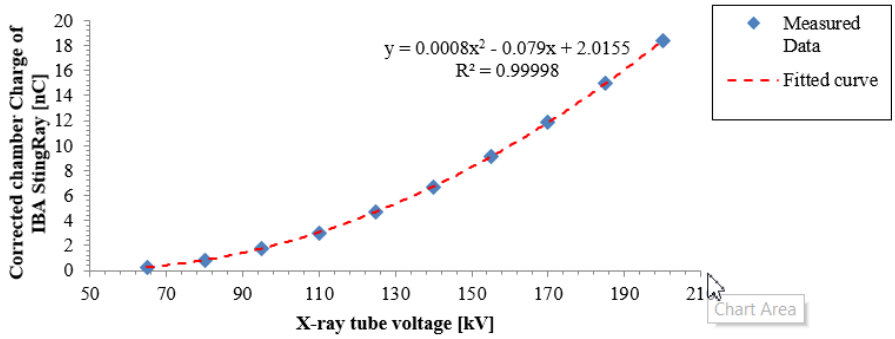

(a) Plot of results of nominal tube voltage dependence of IBA StingRay chamber SN91 with quadratic fitted curve. On the x-axis is the X-ray tube voltage and on the y-axis is the temperature and pressure corrected IBA StingRay charge.

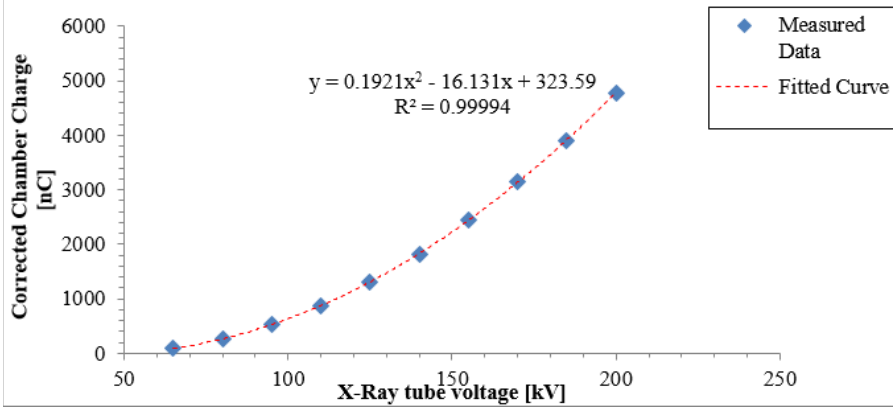

(b) Plot of results of nominal tube voltage dependence of PTW 34089 chamber with quadratic fitted curve. On the x-axis is the X-ray tube voltage and on the y-axis is the temperature and pressure corrected PTW 34089 chamber charge

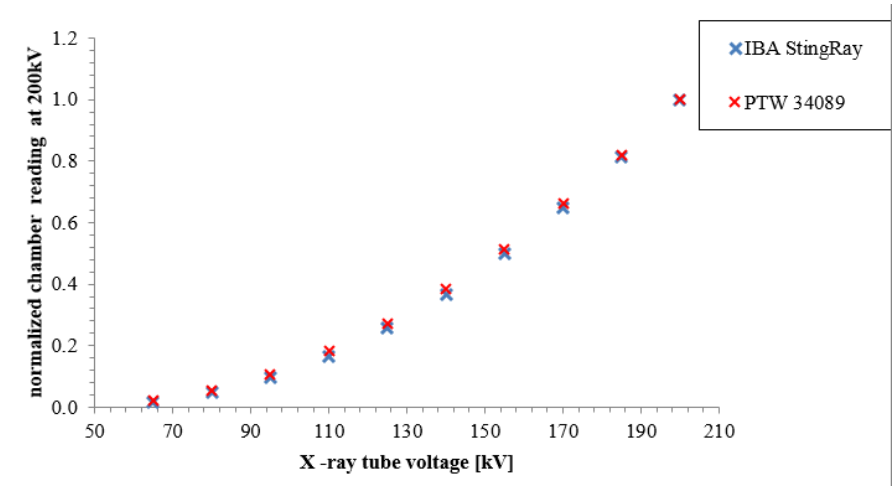

(c) Comparison of results of nominal tube voltage dependence of IBA StingRay SN91 chamber and PTW 34089 chamber with normalized chamber reading at 200 kV.

Figure 4.9: Plotted results for nominal tube voltage dependence of IBA StingRay SN91 and PTW 34089 as well as a comparison of the two chambers.

4.3 Recombination effect

The different regions like plateau region, Bragg peak region and fall off of a carbon ion beam is depicted in figure 3.7b.
The initial as well as the volume recombination are calculated based on the equation 1.10, which is described in section 1.7.1.

4.3.1 Results in the plateau of the beam

The data of the plateau for a carbon ion beam with energy of 346.6 MeV per amu are plotted in figure 4.10 and the calculated initial and volume recombination is shown in table 4.5.
The data of the measurements with carbon ion beam with an energy of 120 MeV per amu are plotted in figure 4.11 and the calculated initial and volume recombination is shown in table 4.6.
The initial recombination as well as the volume recombination were positive for all investigated dose rates. The initial recombination was approximately 0.1% for carbon ions with an energy of 346.6 MeV per amu and 0.2% for 120 MeV per amu within the investigated dose rates. The volume recombination increased with the degrader from 0.01% up to 0.06% for 346.6 MeV per amu and from 0.02% up to 0.09% for 120 MeV per amu.
Overall was the initial recombination as well as the volume recombination higher for 120 MeV per amu than for 346.6 MeV per amu. The uncertainty was less for 120 MeV per amu than for 346.6 MeV per amu.

n	initial recombination[%]	volume recombination at deg20 [%]	volume recombination at deg100[%]
1.5	0.16	0.01	0.04
2	0.04	0.01	0.06
3	0.13	0.01	0.04

Table 4.5: calculated initial and volume recombination for IBA StingRay SN91 with carbon ion beam energy 346.6 MeV per amu in plateau region, which is shown in figure 3.7b

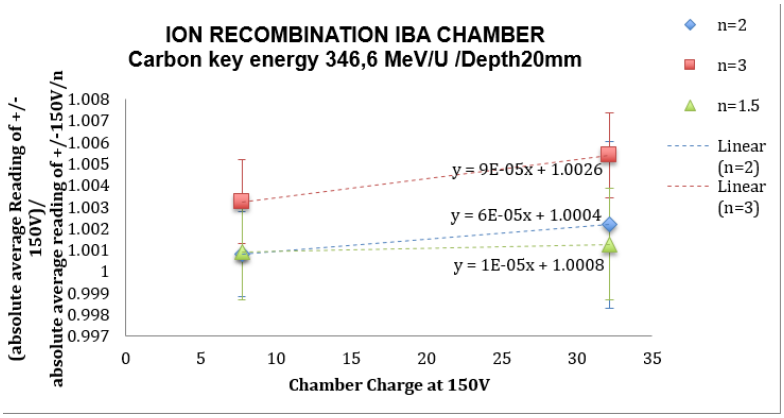

Figure 4.10: Ratio of IV and IV/n for three voltage divisions with linear fits for carbon ion beam energy 346.6 MeV per amu in plateau region, which was in a depth of 20 mm (Measurement series I)

n	initial recombination[%]	volume recombination at deg20 [%]	volume recombination at deg100[%]
1.5	0.24	0.02	0.09
2	0.19	0.02	0.08
3	0.23	0.02	0.09

Table 4.6: calculated initial and volume recombination for IBA StingRay SN91 with carbon ion beam energy 120 MeV per amu in plateau region

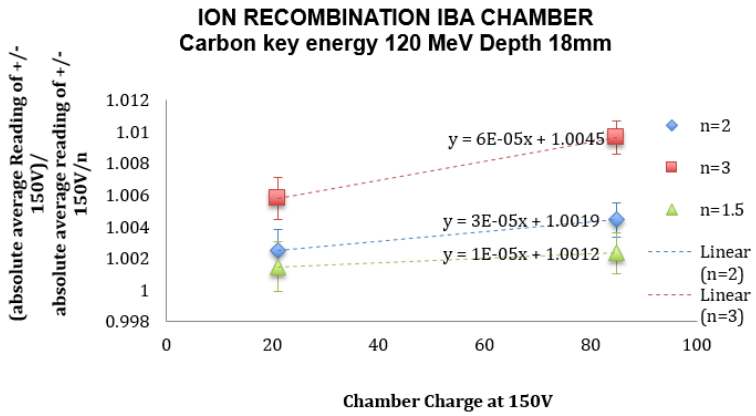

Figure 4.11: Ratio of IV and IV/n for three voltage divisions with linear fits for carbon ion beam energy 120 MeV per amu in plateau region, which was in depth of 18 mm (Measurement series I)

4.3.2 Results at the Bragg peak of the carbon ion beam

The data at the Bragg peak of the carbon ion beam, which is depicted in figure 3.7b, are plotted for the two different carbon key energies in figures 4.12, 4.13 and 4.14. The calculated initial and volume recombination is listed in tables 4.7, 4.8 and 4.9.
The measurements at the peak from measurement series I showed a higher initial recombination than in the plateau, so for carbon ion beam energy of 346.6 MeV per amu and of 120 MeV per amu it was approximately 1.3%. According the model, the B-parameter was negative, which leads to a calculated negative volume recombination from -0.03% up to -0.71%.

n	initial recombination[%]	volume recombination at deg20[%]	volume recombination at deg100[%]
1.5	1.2	-0.09	-0.37
2	1.5	-0.18	-0.71
3	1.12	-0.03	-0.37

Table 4.7: calculated initial and volume recombination for IBA StingRay SN91 with carbon ion beam energy of 346.6 MeV per amu at the Bragg peak (Measurement series I)

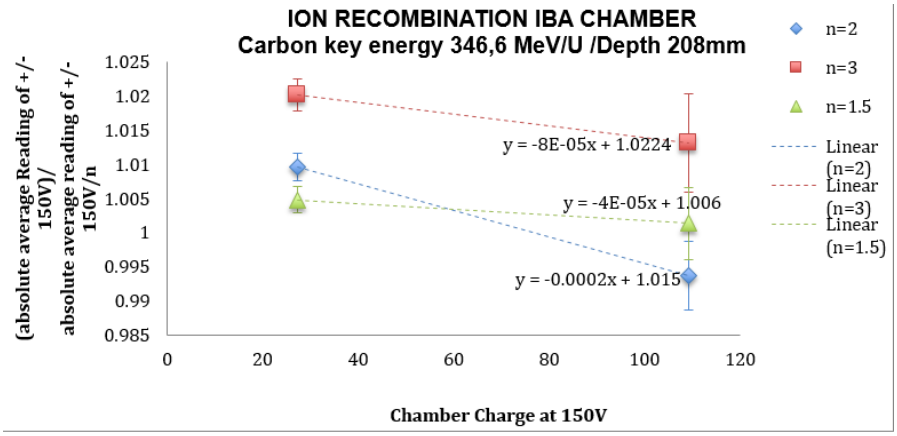

Figure 4.12: Ratio of IV and IV/n for three voltage divisions with linear fits for carbon ion beam energy of 346.6 MeV per amu at the Bragg peak, which was in the depth of 208 mm (Measurement series I)

n	initial recombination[%]	volume recombination at deg20[%]	volume recombination at deg100[%]
1.5	1.51	-0.09	-0.35
2	1.12	0.01	0.02
3	1.32	0.02	0.07

Table 4.8: calculated initial and volume recombination for IBA StingRay SN91 with carbon ion beam energy of 120 MeV per amu at the Bragg peak (Measurement series I)

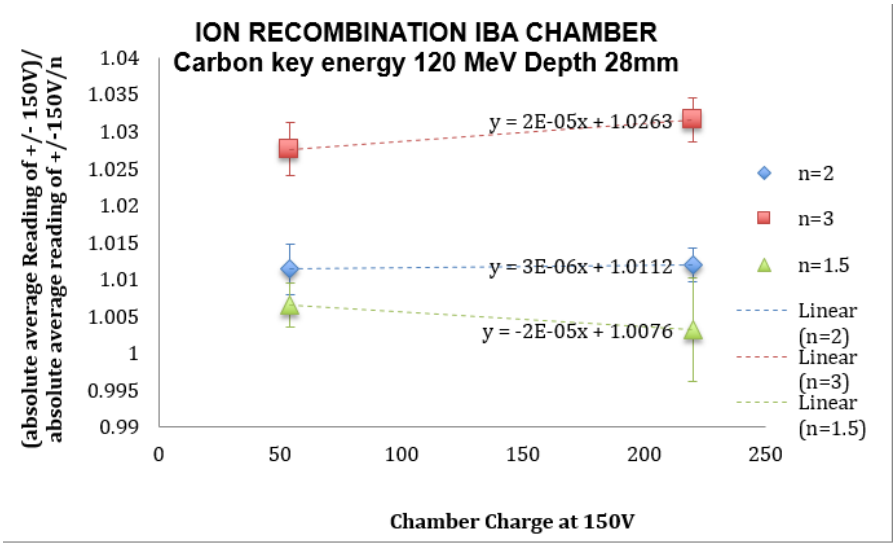

Figure 4.13: Ratio of IV and IV/n for three voltage divisions with linear fits for carbon ion beam energy of 120 MeV per amu at the Bragg peak, which was in a depth of 28 mm (Measurement series I)

n	initial recombination[%]	volume recombination at deg20[%]	volume recombination at deg50[%]	volume recombination at deg100[%]
2	1.27	0.01	0.02	0.03
3	1.27	0.02	0.05	0.08
6	1.05	0.02	0.06	0.09

Table 4.9: calculated initial and volume recombination for IBA StingRay SN91 with carbon ion beam energy of 120 MeV per amu at the Bragg peak, which was in a depth of 27.5 mm (Measurement series II)

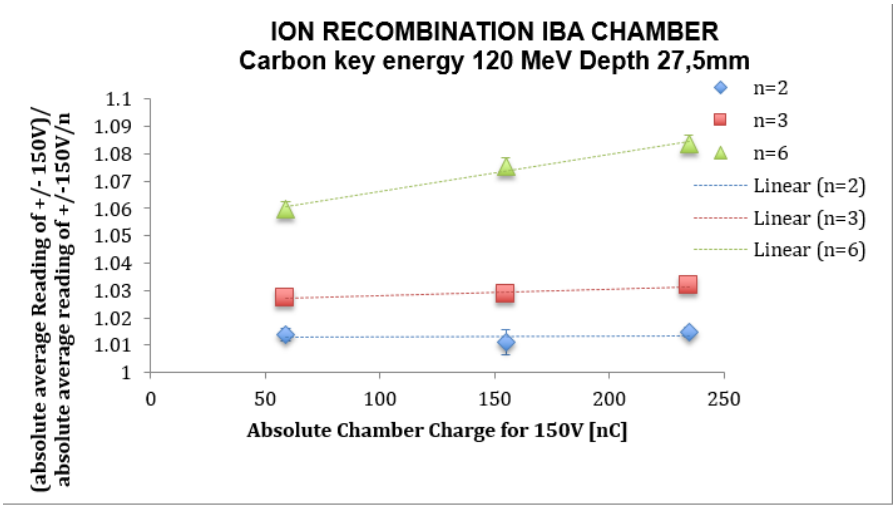

Figure 4.14: Ratio of IV and IV/n for three voltage divisions with linear fits for carbon ion beam energy of 120 MeV per amu at the Bragg peak (Measurement series II)

A comparison of measurement series I and II shows that initial recombination as well as the volume recombination were comparable for carbon ion beam energy of 120 MeV per amu (except for the negative slope from n=1.5 from measurement series I). The calculated initial recombination was 1.32% for measurement series I and 1.20% for measurement series II. The B-parameter of the model was for some measurement points negative, which leads to a calculated volume recombination from -0.35% up to 0.07% for measurement series I and 0.01% up to 0.09% for measurement series II.

Results at the Bragg peak with 120 MeV per amu without ripple filter

The data of the results at the Bragg peak with carbon ion beam energy of 120 MeV per amu without ripple filter are shown in figure 4.15 and the calculated initial and volume recombination is shown in table 4.10.
The result of the initial recombination was approximately 1.4% and the volume recombination increased from 0.0% up to 0.21% without ripple filter. If the results with and without ripple filter from measurement series II were compared, it showed that the initial recombination with ripple filter was $1.20 \pm 0.10\%$ and the initial recombination without ripple filter was $1.36 \pm 0.22\%$. The volume recombination of measurements with ripple filter was between 0.01% and 0.09%, whereas the volume recombination of measurements without ripple filter was fluctuating between 0% and 0.21%.

n	initial recombination[%]	volume recombination at deg20 [%]	volume recombination at deg50 [%]	volume recombination at deg100[%]
2	1.36	0.05	0.13	0.21
3	1.62	0.00	0.01	0.02
6	1.09	0.05	0.12	0.19

Table 4.10: calculated initial and volume recombination for IBA StingRay SN91 with carbon ion beam energy of 120 MeV per amu in Bragg peak without ripple filter(Measurement series II)

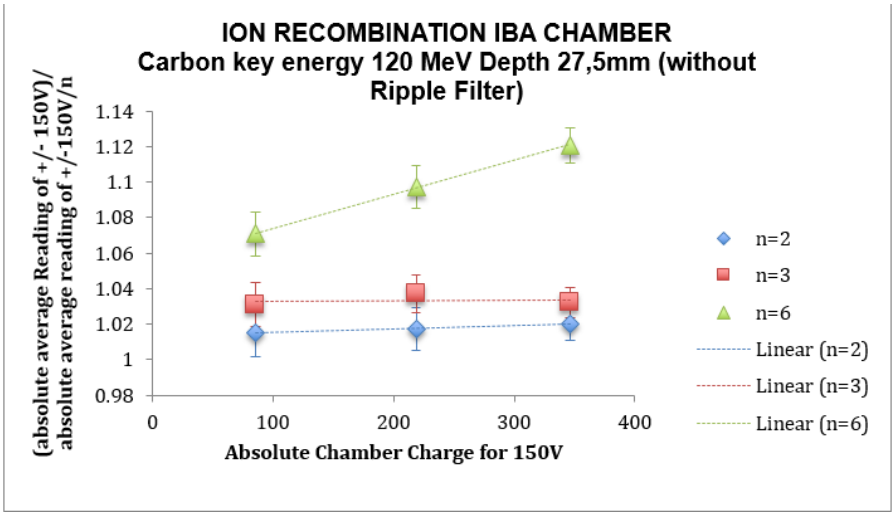

Figure 4.15: Ratio of IV and IV/n for three voltage divisions with linear fits for carbon ion beam energy of 120 MeV per amu without ripple filter at the Bragg peak (Measurement series II)

4.3.3 Results in fall off region of the beam

The data in the fall off region of the beam are plotted in figure 4.16 and figure 4.17. The calculated initial ion recombination and volume recombination is listed in tables 4.11 and 4.12.
The data showed high fluctuations in the fall off region of the beam for measurements with carbon ion beam energy of 346.6 MeV per amu and of 120 MeV per amu.
Table 4.11 shows that the initial recombination was low and holds negative values (up to -5.31%) for measurements with carbon ion beam energy of 346.6 MeV per amu. Moreover,the dose rate for degrader 100 for n=2 was higher than for n=3. For measurements with carbon ion beam energy 120 MeV per amu the initial recombination was approximately 1.35% and the B-parameter of the model was negative, due to the negative slope

of the dose rates (Refer to table 4.12). Figure 4.17 depicts that the dose rate for degrader 100 and n=1.5 is higher than for n=2.

n	initial recombination[%]	volume recombination at deg20[%]	volume recombination at deg100[%]
1.5	0.02	-0.22	-1.05
2	-5.31	1.72	8.13
3	-0.06	0.21	0.98

Table 4.11: calculated initial and volume recombination for IBA StingRay SN91 with 346.6 MeV per amu in fall off region of the beam (Measurement series I)

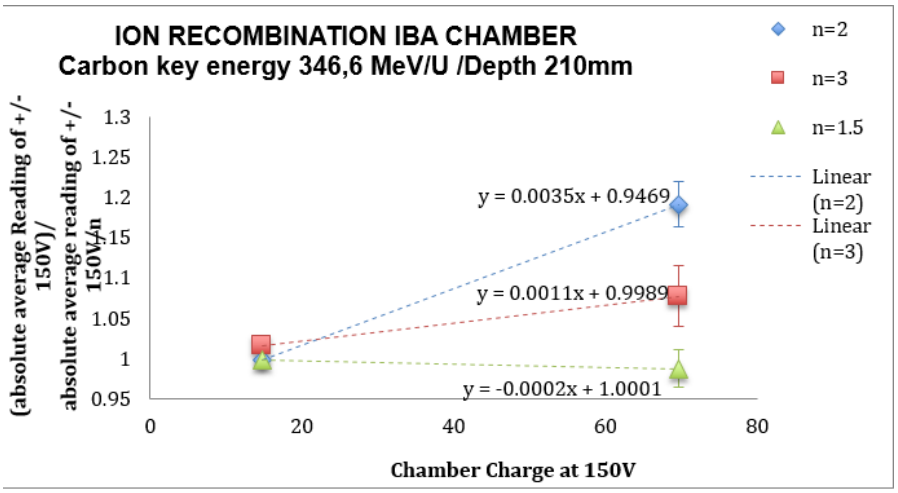

Figure 4.16: Ratio of IV and IV/n for three voltage divisions with linear fits for carbon ion beam energy 346.6 MeV per amu in fall off region of the beam, which was in a depth of 210 mm(Measurement series I)

n	initial recombination[%]	volume recombination at deg20[%]	volume recombination at deg100[%]
1.5	1.09	-0.17	-0.67
2	1.07	-0.18	-0.69
3	1.89	-0.08	-0.31

Table 4.12: calculated initial and volume recombination for IBA StingRay SN91 with carbon ion beam energy of 120 MeV per amu in fall off region of the beam(Measurement series I)

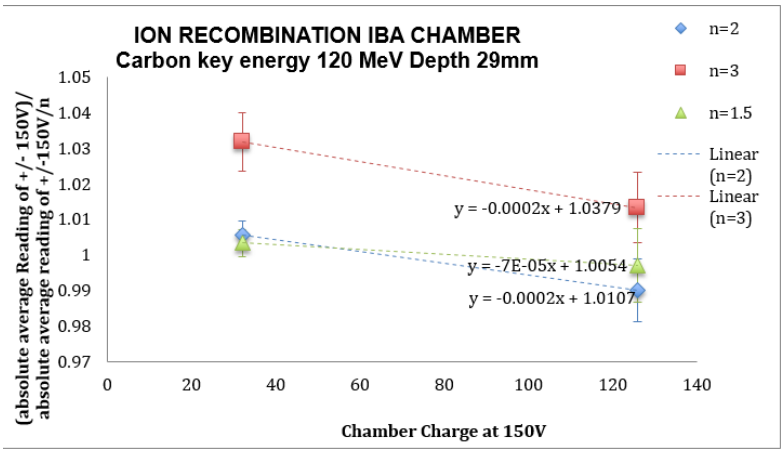

Figure 4.17: Ratio of IV and IV/n for three voltage divisions with linear fits for carbon ion beam energy of 120 MeV per amu in fall off region, which was in a depth of 29 mm (Measurement series I)

4.3.4 Results for lateral offsets

Ion recombination measured at lateral offsets of +30 mm and -30 mm with carbon ion beam energy of 346.6 MeV per amu and Degrader 100 at the peak and fall off region. The figure 4.18 shows the dependencies from inverse of the absolute average of positive and negative reading against of the inverse of the squared of Ionisation chamber voltage. The results of the peak as well as the results of the fall off were fluctuating for the different offsets.

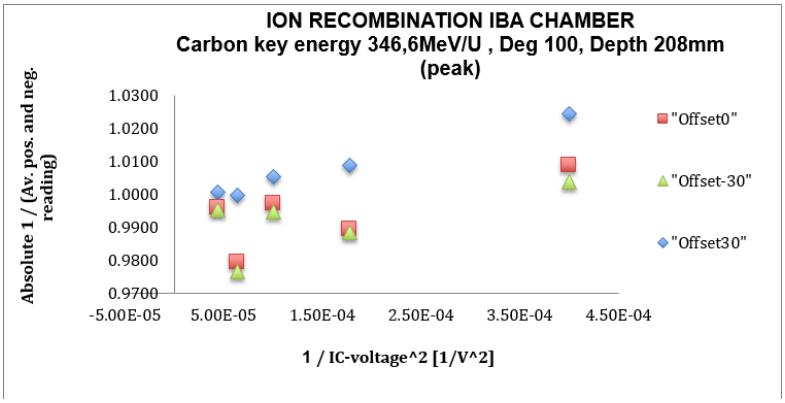

(a) Inverse of the ionization current plotted against the inverse square of the polarizing voltage for the peak with carbon ion beam energy of 346.6 MeV per amu

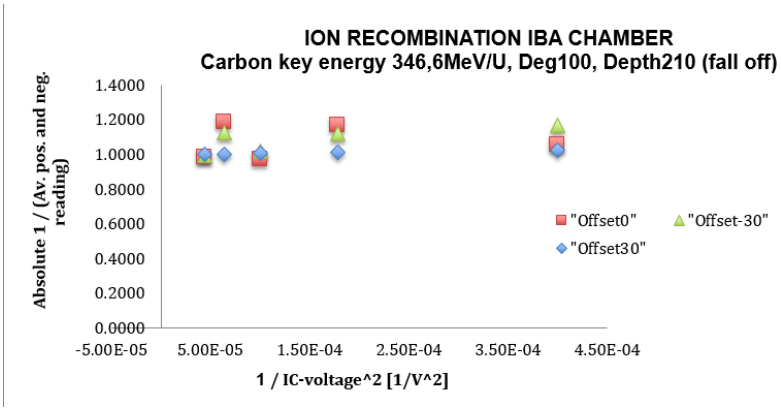

(b) inverse of the ionization current plotted against the inverse square of the polarizing voltage for the fall off with carbon ion beam energy of 346.6 MeV per amu

Figure 4.18: Plotted results for lateral offsets with carbon ion beam energy of 346.6 MeV per amu

CHAPTER 5

Discussion

A newly-designed large-area plane-parallel ionization chamber IBA StingRay with a nominal active volume diameter of 120 mm is characterized in this thesis. Such large-area plane-parallel ionization chambers show benefits compared to smaller chambers in the field of scanned light-ion beam dosimetry. They increased radius of the chamber increases the geometric collection efficiency depending on beam energy and depth [8] and it eases positioning with respect to small fields [31]. Hanusova used the IBA StingRay for a gamma spectrometry study and tested the activation of quality assurance devices and phantom materials under clinical scanning proton beams [22]. Two IBA StingRay chambers (SN91 and SN93) were investigated in the particle therapy center MedAustron and compared in this study.

The main focus of this work was on the response homogeneity of the chambers and the ion recombination effects. For the ion recombination effects the theories of Boag and Jaffe were considered.

The lateral response of the IBA StingRay chamber SN91 and SN93 were measured with different methods and two beam qualities (i.e X-rays and proton beams).

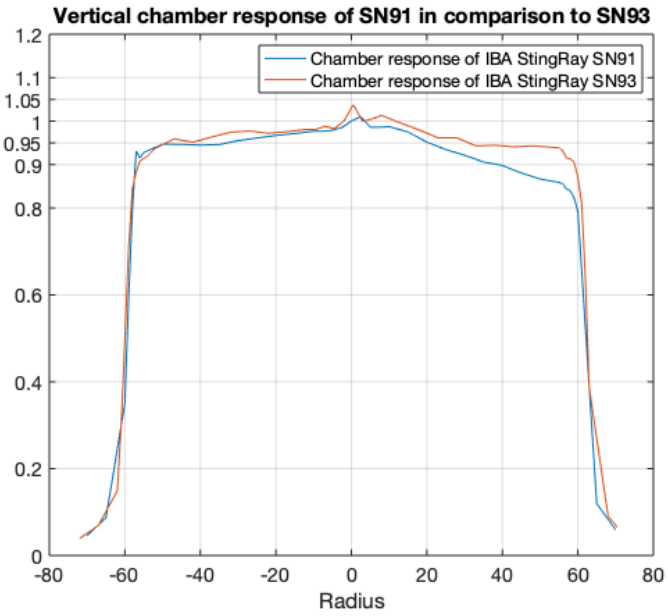

(a) Comparison of vertical profile of IBA StingRay SN93 and SN91 with X-ray beam

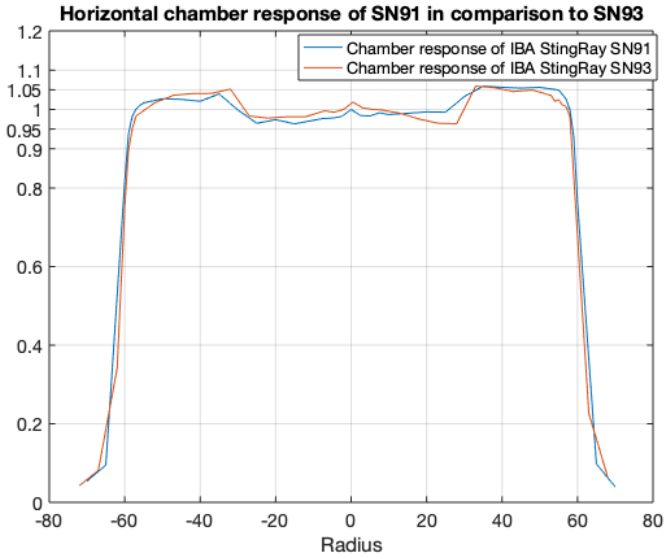

(b) Comparison of horizontal profile of IBA StingRay SN93 and SN91 with an X-ray beam

Figure 5.1: Comparison of vertical and horizontal profile of SN93 and SN91 with an X-ray beam

Figure 5.1 shows a comparison of the vertical and horizontal response of the IBA StingRay SN91 and SN93 measured with an X-ray beam.
Figure 5.1b depicts the horizontal response of both chambers (IBA StingRay SN91 and

SN93) when measured with an X-ray beam. It showed an increase of the chamber response normalized to the chamber center by approximately +5% towards the edges (between chamber radius ±35 mm up to ±60 mm).
This increase is likely caused due to the screws at the edges of the IBA StingRay chamber (see figure 5.2), which were creating a photoelectric effect, due to this "spikes" in the response pattern no edge correction was applied for the measurements in X-rays as an edge correction is only meaningful when the region close to the edge is measured correctly.

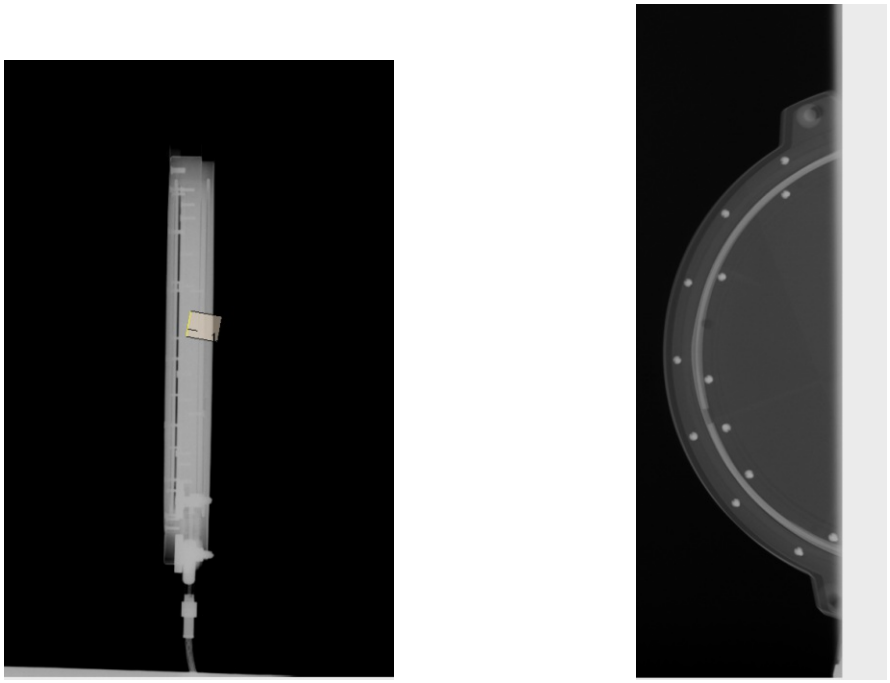

(a) X-ray image of the side view of the IBA StingRay SN91

(b) X-ray image of the half of the front view of the IBA StingRay SN91

Figure 5.2: X- ray images of IBA StingRay SN91

Figure 5.1a depicts a comparison of the chamber response of the vertical axis for IBA StingRay SN91 and SN93 measured with an X-ray beam, which had its maximum at the center of the IBA StingRay for both of the investigated chambers. The vertical response of IBA StingRay chambers SN91 and SN93 had no increase between chamber radius ±35 mm and ±60 mm, but the vertical response of SN91 was lower by -3.4% between a chamber radius of 40 mm and 60 mm than between a negative chamber radius of -40 mm and 60 mm. The vertical response of SN93 did not show this decrease along the edges (see figure 5.1a). This effect may have happened due to the fact that the IBA StingRay chamber was not completely parallel to the source and its reference chamber. So maybe the airgap between the two electrodes of the IBA StingRay was not constant within the chamber.

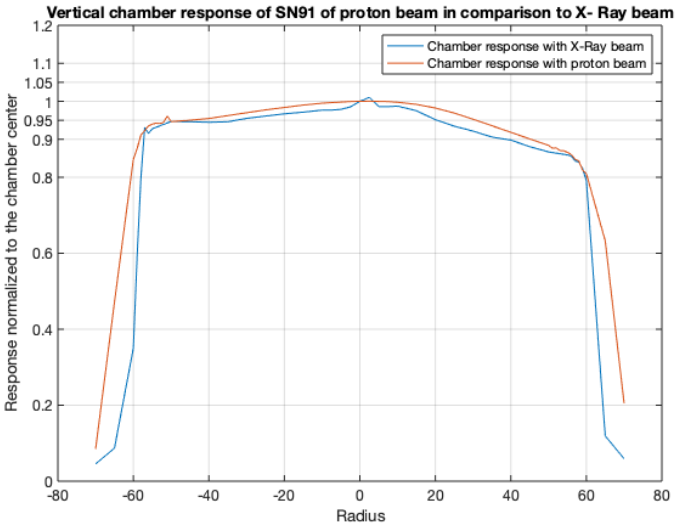

(a) Comparison of vertical profile of IBA StingRay SN91 measured with an X-ray beam and a proton beam

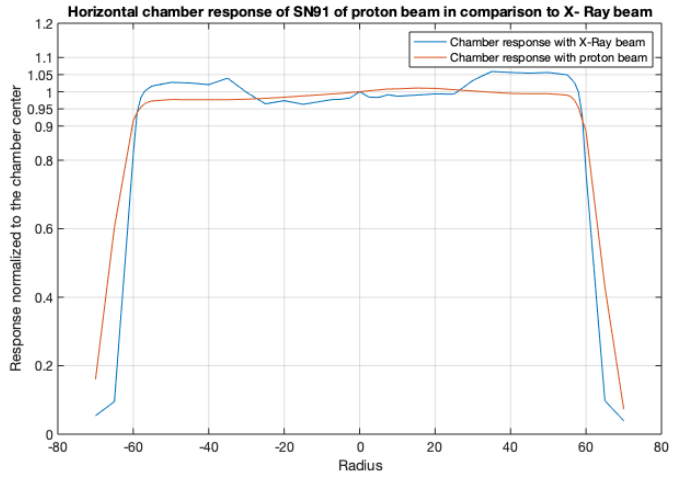

(b) Comparison of horizontal profile of IBA StingRay SN91 measured with a proton and an X-ray beam

Figure 5.3: Comparison of vertical and horizontal profile of IBA StingRay SN91 measured with an X-ray beam and a proton beam

When comparing horizontal profiles of IBA StingRay SN91 measured with an X-ray beam and a proton beam it shows that for the results measured with a proton beam there was no increase, but a decrease by 2-3% of the normalized response to the chamber center along the edges (see figure 5.3b).

The comparison of vertical profiles of IBA StingRay measured with a proton beam and X-ray beam is depicted in figure 5.3a and shows the same trend of the profiles from the chamber center up to $pm60$ mm of the chamber radius. This is an element, which is arguing against Goma's assumed hypothesis, which quotes that the profiles measured with an X-ray beam are not representative for those which are measured with a proton beam.

An edge correction was only applied for lateral responses of the chambers, which were measured with a proton beam. Therefore a margin of 0.5 mm was used for the radius of the active area within this study. The value of the margin was derived by studying the corrected edge response. Values between 0 to 0.6 mm were checked. With smaller values than 0.5 mm an unexplained over-response of the chamber at the edges was noted. With higher values than 0.5 mm an under response was observed. Over all the margin was chosen to get a realistic behaviour without any change of the response at the edges of the chamber [31].

The deviation in response differed between the two investigated specimen of this chamber type. The response of the star pattern profile of IBA StingRay SN91 normalized to the chamber's center measured with an X-ray beam (details see chapter 4.1.4) had within the active area of the chamber a maximum deviation of 13% (Figure 4.4), whereas the the maximum deviation of the IBA StingRay SN93 was up to 6% (Figure 4.5.

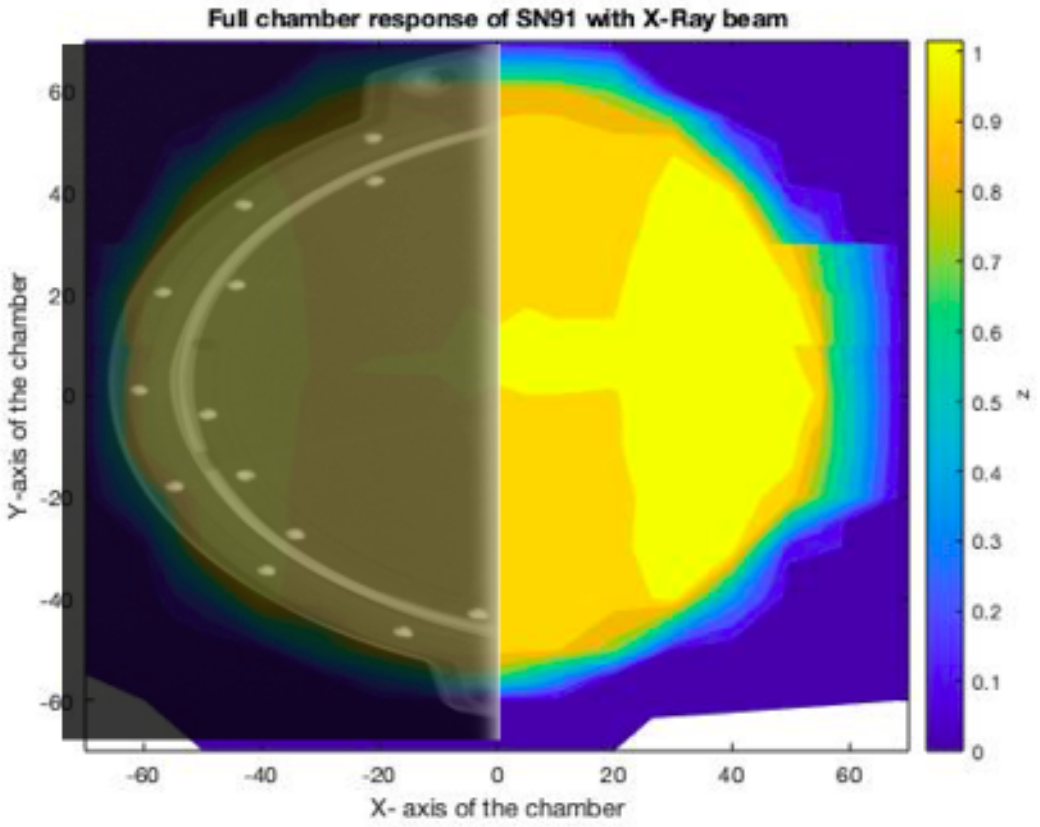

Figure 5.4: Overlay of X-ray of IBA StingRay SN91 with full profile dose response map

The full chamber profile response of IBA StingRay SN91 (Figure 4.6a) measured with an X-ray beam had a decrease of the response at the vertical axis at chamber radius 40 mm up to 60 mm, which was not present in the full profile response of IBA StingRay SN93 (see Figure 4.6b). Figure 5.4 shows the response of IBA StingRay SN91 measured with an X-ray beam superimposed with an X-ray image of the IBA StingRay SN91. It depicts an increase of the response along the left and right side edges of the IBA StingRay SN91, which is related to the screws located along the area where the response increase happened.

A comparison of the homogeneity of the IBA StingRay chamber with other large area ionization chambers from different studies was done. Therefore the IBA StingRay chamber was compared with the PTW34089, also denoted as BPC150, which has an active volume diameter of 147 mm and which was investigated by Kuess et al (2017,2019 and 2020) [40][41][31]. The homogeneity of the BPC150 was measured with a proton and X-ray beam. The radial response map, gathered with a proton beam, showed that the response in the center of the chamber is 3% lower than the average response over the total active area. It was not possible to measure the complete chamber response of the BPC150 with

the X-ray beam due to the holder of the chamber and also backscatter occurred. The IBA StingRay did not show the problem with the holder, so it was possible to measure the complete response with the X-ray beam.
In the study of Kuess et al 2017 8 different large area ionization chambers with thick and thin window were compared. The study showed that thick window chambers had a response decrease at the chamber edges, whereas thin window chambers had an increase at the chamber edges[40]. This paper from Kuess et al 2017 was also discussed and commented within Kuess et al 2019 [41]. It quotes that there is an expected decrease of the response homogeneity of approximately 2% at the edges, because of the average range of secondary electrons, which is about 4 cm. So if there is an area at the chamber which is not centrally irradiated, then some of the secondary particles are passing the chamber and are not detected. This is a symmetric behaviour and leads to the expectation that the response at the edges should be decreased [41]. But this does not explain the variation between the thick and thin window chambers.

Some functional tests of the IBA StingRay SN91 were measured with an X-ray beam. In detail polarity effect, dose stability, dose rate stability and beam quality dependence were investigated [39].
Table 4.1 shows the polarity effect of the IBA StingRay chamber with an maximal k_{pol} of 1.2%, which is quite high and should not be neglected as quoted by Mirandola et al 2019 [38]. Mirandola et al (2019) investigated polarity and ion recombination effects for a similar chamber, i.e. PTW 34080, for proton and carbon ion beams. It was shown that polarity effects can be neglected as well as ion recombination effects for proton beams. For carbon ion beams the ion recombination is LET depending, ranging from 1.000 to 1.040 (Mirandola et al 2019) [38].
The polarity effect can be induced due to currents which are collected outside of the sensitive volume of the ionization chamber [45][30][46]. Also the manufacturing process can be the cause, which is shown by McEwen et al [35].

The IBA StingRay dose stability results are shown in table 4.2 and figure 4.7 and showed a linear behaviour as expected. Also the other functional tests of IBA StingRay SN91, like dose rate stability (see figure 4.8 and table 4.3) and beam quality dependence (see figure 4.9 and table 4.4) with X-ray beam had no unexpected behaviour.

The Ion recombination of IBA StingRay SN91 was measured at two measurement series (Measurement series I and measurement series II) for two different carbon ion beam energies of 120 MeV per amu and 346.6 MeV per amu. Three regions, like the plateau region, Bragg peak and fall off region, were measured with different degrader settings and some of them with and without ripple filter. In addition different lateral offsets were investigated, details see section 3.3. For measurement series I we measured only two degrader settings. For measurement series II we increased it to three degrader settings, which improved the trend of the plots of the ratio of IV and IV/n and the calculated recombination factors. Moreover it should be mentioned that all data were documented

manually in an excel list but double checked with the double eye principle.

If you have a deeper look at the results of the recombination measurements, the tables 4.6 and 4.5 show that the calculated initial ion recombination effect of the plateau region of the beam was about 0.11% for an carbon ion beam energy of 346.6 MeV per amu and about 0.22% for 120 MeV per amu. The calculated volume recombination was between 0.01% and 0.06% for a carbon ion beam energy of 346.6 MeV per amu and between 0.02% and 0.09% for 120 MeV per amu. So all results were in a positive range and the recombination with an carbon ion beam energy of 120 MeV per amu was higher than for an energy of 346.6 Mev per amu.

When comparing the recombination effect of the IBA StingRay SN91 at the Bragg peak for different carbon ion beam energies, it shows that the initial recombination for a carbon ion beam energy of 346.6 MeV per amu and 120 MeV per amu was approximately 1.3%. So the initial recombination at the peak was by approximately 1% higher than in the plateau region. The calculated volume recombination at the peak with carbon ion beam energy 346.6 MeV per amu (see table 4.7) resulted into negative values, due to a negative B-parameter in the model, hence it must be influenced by another effect than volume recombination[21].

So for further analysis of the in peak measurement, we derived the volume recombination for higher intensities from the data in the plateau region. The constant part of recombination is related to the initial recombination, the volume recombination is dependent on dose rate. In other words, the slopes of the fits were fixed based on the plateau region data and only the intercept was a free parameter which was fitted based on the data from peak. Thus for measurements at the Bragg peak with Carbon key energy of 346.6 MeV per amu following results were derived with the fitting to table 5.1 and plot 5.5:

n	initial recombination[%]	volume recombination at deg20[%]	volume recombination at deg100[%]
1.5	1.1996	0.0324	0.1295
2	1.12055	0.03	0.1199
3	1.5018	0.0503	0.2013

Table 5.1: calculated initial and volume recombination for IBA StingRay SN91 with carbon ion beam energy of 346.6 MeV per amu at the Bragg peak (Measurement series I)

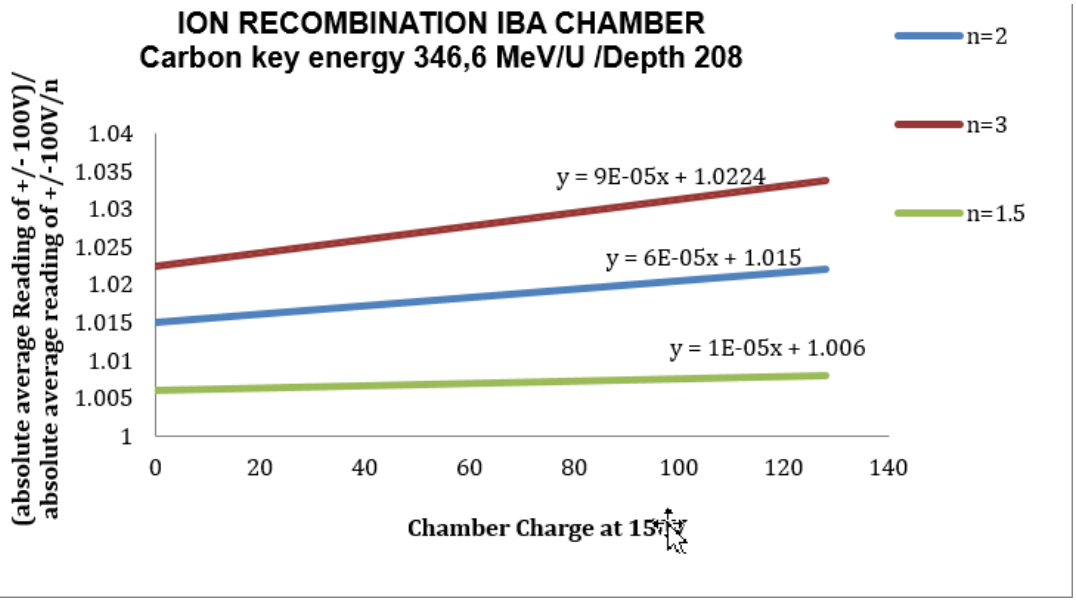

Figure 5.5: Ratio of IV and IV/n for three voltage divisions with linear fits for carbon ion beam energy of 346.6 MeV per amu at the bragg peak (Measurement series I) with fixed slopes based on the data of the plateau measurements

When comparing the data of the peak with a carbon ion beam energy of 120 MeV per amu for the two different measurement series I and II with inserted ripple filter(see table 4.9 and 4.8) it shows that the results are very similar and comparable.

If you have a look at the data of the fall off region it is shown in tables 4.12 and 4.11, you can see that data of the fall off were highly fluctuating, so we checked this behaviour only at measurement series I because the recombination effect was very small. If the results of the IBA StingRay chamber are compared with different literature, it shows that the calculated volume recombination of IBA StingRay SN91 was all in all very low, in comparison to other chambers like a Markus Chamber or a Roos chamber, which were investigated by Palmans et al 2006 in a clinical 60 MeV passive proton beam of the Clatterbridge Centre of Oncology at typical dose rates of 26 $Gy\ min^{-1}$. Palmans found for the Markus chamber a correction of 0.8% at the centre of the Bragg peak with an operation voltage of 100 V. The recombination resulted from 0.3% initial recombination and 0.5% from volume recombination [24].

CHAPTER 6

Conclusion and Outlook

The aim of this thesis was to investigate two specimen of the IBA StingRay chamber. The plane parallel large area ionization chamber with an diameter of the active area of 120 mm has an high collecting efficiency due to increased active diameter in comparison to other commercially available Bragg peak chambers with exception of the PTW150. The behaviour of the IBA StingRay chambers was tested with X-rays, proton, and carbon ion beams.

From the center to ±30 mm of the radius lateral response of the IBA StingRay was stable. From ±30 mm radius onwards it increased for the horizontal response until the edges whereas for the vertical response did not increase.

If the lateral response of proton and X-ray beam are compared, a similar behaviour was observed, except for some X-ray back scatter which happened along the edges due to the screws of the IBA StingRay (see figure 5.2 and 5.4).

A comparison of the IBA StingRay with PTW chambers showed that the response behaviour of the IBA StingRay is similar to the measurement results of the PTW chambers. So all in all there is no noticeable advantage or disadvantage which differentiate between PTW or IBA chambers.

To allow a deeper analysis further measurements should be conducted focusing on the ion recombination effects. It would be interesting to repeat the measurements for recombination effect with the IBA StingRay SN93 and also other large area ionization chambers from different vendors than IBA. Furthermore it would be of interest to compare the measurements of the lateral response with Monte Carlo simulations.

CHAPTER 7

Appendix

7.1 Temperature and Pressure correction

The temperature and pressure correction is applied on the electrometer reading M, which is gathered in electrical units. The electrometer reading is corrected due to aberration from reference temperature $T_0 = 20°C$ and pressure $P_0 = 1013hPa$. The corrected electrometer reading M_{corr} is calculated in the following way:

$$M_{corr} = k_{TP} * M \tag{7.1}$$

$$k_{TP} = \frac{273.2 + T}{273.2 + T_0} * \frac{P_0}{P} \tag{7.2}$$

For Yxlon X-ray unit measurements, the Temperature T and the pressure P are recorded inside the steel container. As the door of the Yxlon cannot be opened during irradiation, the recording is done before and after each measurement and a linear relationship is assumed. The interpolated values are used as k_{TP}
For measurements with the proton beam, the temperature and the pressure of the proton irradiation room (IR1) is recorded in real time via video surveillance.

7.2 Certificates

Certificate of Compliance and Calibration

This document certifies that the
DOSE 1 Reference Grade Therapy Dosimeter

Serial No.: - 20591 -

complies with the International Standard IEC 60731 second edition 1997-07

Charge calibration is expected to be accurate within an initial tolerance of ±0,1%.

The accuracy and calibration are traceable to international standards through calibration equipments which are tested and calibrated on a regular basis in comparison with reference standards at approved National Metrology Laboratories.

The manufacturer operates a certified quality management system according to the following standards

EN ISO 13485 / 07.2003

11.02.2020
Date

Service Engineer

FOA/PE D1000-2/7/01-11

Figure 7.1: Certificate of IBA DOSE 1

iba

Certificate of Compliance

This document certifies that the

Stingray ionization chamber

Serial Number: 0091

meets or exceeds specifications published by IBA Dosimetry GmbH as stated in the referenced procedure.

Water equivalent thickness of the entrance window:	5.06 mm
Average height of the pin tips:	4.53 mm
Standard measurement uncertainty:	0.03 mm

It has been tested using measurement laboratory standards traceable to the recognized National Metrology Institutes and other reference national laboratories standards.

The manufacturer operates certified quality management system according to the following standards

EN ISO 13485:2016
EN ISO 17025:2005

Procedures used for testing:
WI_DL_CAL_Stingray_028 and WI_MF_Large_Chamber_001

Date of testing	Testing approved by	Testing performed by
05.08.2019	Deputy of Head of the calibration laboratory	Calibration Manager

Certificate of Compliance without signature is not valid. It shall not be reproduced except in full without any approval of IBA Dosimetry.

TP_DL_CAL_Stingray_028-1_Rev06

IBA Dosimetry GmbH

Figure 7.2: Certificate of IBA StingRay chamber with serial number 91

Certificate
of
Compliance

This document certifies that the

Stingray ionization chamber

Serial Number: 0093

meets or exceeds specifications published by IBA Dosimetry GmbH as stated in the referenced procedure.

Water equivalent thickness of the entrance window:	4.94 mm
Average height of the pin tips:	4.68 mm
Standard measurement uncertainty:	0.03 mm

It has been tested using measurement laboratory standards traceable to the recognized National Metrology Institutes and other reference national laboratories standards.

The manufacturer operates certified quality management system according to the following standards

EN ISO 13485:2016
EN ISO 17025:2005

Procedures used for testing:
WI_DL_CAL_Stingray_028 and WI_MF_Large_Chamber_001

Date of testing	Testing approved by	Testing performed by
13/08/2019	Head of Dosimetry Laboratory	Calibration Manager

Certificate of Compliance without signature is not valid. It shall not be reproduced except in full without any approval of IBA Dosimetry.

TP_DL_CAL_Stingray_028-1_Rev06

Figure 7.3: Certificate of IBA StingRay chamber with serial number 93

List of Figures

List of Tables

Bibliography

[1] Abdullah, K. M. S. *Fundamentals in nuclear physics*. University of Duhok under the authorization of Directorate of Libraries in Duhok/ Kurdistan Region-Iraq, 2014.

[2] AGENCY, I. A. E. Cyclotron produced radionuclides: Principles and practice. Tech. rep., International atomic energy agency, Vienna, 12 2008.

[3] Andrew Nisbet, D. I. T. Polarity and ion recombination correction factors for ionization chambers employed in electron beam dosimetry. *Physics in Medicine Biology* (1998).

[4] Attix, F. H. *Introduction to radiological physics and radiation dosimetry*. WILEY-VCH Verlag GmbH Co. KGaA, 1986.

[5] Boag. Ionization chambers radiation dosimetry (instrumentation vol ii. In *F H Attix et al*. New York:Academic, 1966, ch. 9.

[6] Bolus, N. E. Basic review of radiation biology and terminology. *J.Nucl.Med. Technol.* (2001).

[7] Cai Grau, Marco Durante, D. G. J. A. L., and Weber, D. C. Particle therapy in europe. *Mol.Oncol* (2020).

[8] Christian Bäumer, Benjamin Koska, J. L. B. T. T. M., and Talla, P. T. Evaluation of detectors for acquisition of pristine depth-dose curves in pencil beam scanning. *Journal of applied clinical medical physics* (2015).

[9] Clelanda, M. R., and Stichelbaut, F. Radiation processing with high-energy x-rays. *Radiation Physics and Chemistry* (2013).

[10] D.R. Dance, S. Christofides, A. M. I. M. K. N. *Diagnostic Radiology Physics: a handbook for teachers and students*. international atomic energy agency, 2014.

[11] Durante, M., and Paganetti, H. Nuclear physics in particle therapy: a review. *IOP Publishing Ltd* (2016).

[12] Faiza Bourhaleb, A. A., and Russo, G. Monte carlo simulations for beam delivery line design in radiation therapy with heavy ion beams. *Applications of Monte Carlo Methods in Biology, Medicine and Other Fields of Science* (2011).

[13] Freiburg, P. *User Manual: Bragg Peak Chambers Type 34070, 34073 and 34080*, 2009.

[14] Freiburg, P. *User Manual: UNIDOSwebline Type 10021, Type 10022 and Type 10023.*, 2014.

[15] Freiburg, P. *Assembly Instructions and User Manual: MP3-P Therapy Beam Analyzer T41029, PT Water Reservoir T41028.*, 2016.

[16] Freiburg, P. *Assembly Instructions and User Manual MP3-PL Therapy Beam Analyzer T41050.*, 2016.

[17] G. Battistoni, I. M., and Muraro, S. Nuclear physics and particle therapy. *Taylor and Francis Group* (2016).

[18] George, J. Zur theorie der ionization in kolonnen. *Annalen der Phyisk* (1913).

[19] GmbH, I. D. *User's Guide. Stingray-Large Ionization Chamber for PBS.* IBA Dosimetry GmbH, Schwarzenbruck, 2019.

[20] GmBH, Y. I. *Betriebsanleitung Y.Solution Maxishot.*, 2013.

[21] Gomà, C. Comment on 'lateral response heterogeneity of bragg peak ionization chambers for narrow-beam photon and proton dosimetry'. 168002.

[22] Hanušová, T., Johnová, K., Navrátil, M., Valenta, J., and Müller, L. Activation of QA devices and phantom materials under clinical scanning proton beams—a gamma spectrometry study. *Physics in Medicine & Biology 63*, 11 (jun 2018), 115014.

[23] Haupt, S. Dose area product measurements with a novel large area ionization chamber in scanned proton beams, 2019.

[24] Hugo Palmans, Russell Thomas, A. K. Ion recombination correction in the clatterbridge centre of oncology clinical proton beam. *Physics in Medicine Biology* (2006).

[25] IBA. Dose 1.

[26] IPEMB. The ipemb code of practice for electron dosimetry for radiotherapy beams of initial energy from 2 to 50 mev based on an air kerma calibration. *Physics in Medicine Biology* (1996).

[27] J Tikkanen, K Zink, M. P. P. T. J. B. J. O. T. S. C. G. M. P. Calculated beam quality correction factors for ionization chambers in mv photon beams. *Physics in Medicine Biology* (2020).

[28] Jerrold T Bushberg, P. The aapm/rsna physics tutorial for residents. x-ray interactions. *Radiographics* (1998).

[29] Jiajian Shen, Xiaoning Ding, Y. H. Y. K. W. L. W. D., and Bues, M. Technical note: Comprehensive evaluation and implementation of two independent methods for beam monitor calibration for proton scanning beam. Tech. rep., Department of Radiation Oncology, USA Phoenix, 10 2019.

[30] Khan, F. M. *Diagnostic Radiology Physics: a handbook for teachers and students*. Lippincott Williams and Wilkins, 2003.

[31] Kuess, P., Haupt, S., Osorio, J., Grevillot, L., Fuchs, H., Georg, D., and Palmans, H. Characterization of the PTW-34089 type 147 mm diameter large-area ionization chamber for use in light-ion beams. *Physics in Medicine & Biology 65*, 17 (sep 2020), 17NT02.

[32] M, B. Volume recombination parameter in ionization chambers. *Phys.Med.Biol.* (1998).

[33] Manninen, A.-L. Clinical applications of radiophotoluminescence (rpl) dosimetry in evaluation of patient radiation exposure in radiology. determination of absorbed and effective dose. *Onco Targets and Therapy* (2016).

[34] Małgorzata Liszka, Liliana Stolarczyk Magdalena Kłodowska, A. K. D. K. N. M. A. P. M. P. R. W. P. O. Ion recombination and polarity correction factors for a plane–parallel ionization chamber in a proton scanning beam. *Medical physics* (2018).

[35] McEwen, M. R., Williams, A. J., and DuSautoy, A. R. Determination of absorbed dose calibration factors for therapy level electron beam ionization chambers. 741–755.

[36] MedAustron. The particle accelerator.

[37] MedAustron. Synchrotron.

[38] Mirandola, A., Magro, G., Maestri, D., Mairani, A., Mastella, E., Molinelli, S., Russo, S., Vai, A., and Ciocca, M. Determination of ion recombination and polarity effect correction factors for a plane-parallel ionization bragg peak chamber under proton and carbon ion pencil beams. *Physics in Medicine and Biology 64* (03 2019).

[39] Moser, V. Commission of iba stingray large area ionization chamber, 2020.

[40] P Kuess, T T Boehlen, W. L. A. E. D. G. H. P. Lateral response heterogeneity of bragg peak ionization chambers for narrow-beam photon and proton dosimetry. *Physics in Medicine Biology* (2017).

[41] P Kuess, T T Boehlen, W. L. A. E. D. G. H. P. Reply to comment on 'lateral response heterogeneity of bragg peak ionization chambers for narrow-beam photon and proton dosimetry'. *Physics in Medicine Biology* (2019).

[42] P.J.Potts. X-ray fluorescence and emission. wavelength dispersive x-ray fluorescence. *Encyclopedia of Analytical Science (Second Edition)* (2005).

[43] Podgoršak, E. *Radiation physics for medical physicists.* Springer internantional, 2016.

[44] Ralf Dreindl, Loic Grevillot, V. L. P. K. A. C. A. E. M. S. S. V. H. P. J. O. Beam monitor calibration for scanned proton and carbon ion beams in a synchrotron based facility – the medaustron experience.

[45] Roos, M., and Derikum, K. The recombination correction and the dependence of the response of plane parallel chambers on the polarizing voltage in pulsed electron and photon beams. Tech. rep., Review of Data and Methods Recommended in the International Code of Practice for Dosimetry„ IAEA TECDOC 1173, 2000.

[46] Rossomme, S., Hopfgartner, J., Lee, N. D., Delor, A., Thomas, R. A. S., Romano, F., Fukumura, A., Vynckier, S., and Palmans, H. Ion recombination correction in carbon ion beams. *Medical Physics 43*, 7 (2016), 4198–4208.

[47] S Rossomme, J Horn, S. B. O. J. A. M. M. C. V. F. F. R. D. R. G. S. V. H. P. Ion recombination correction factor in scanned light-ion beams for absolute dose measurement using plane-parallel ionisation chambers. *Physics in Medicine Biology* (2017).

[48] Sons, J. W. . *Radiation Therapy Physics.* 2013.

[49] Yamoah, K., and Johnstone, P. A. Proton beam therapy: clinical utility and current status in prostate cancer. *Onco Targets Ther.* (2016).

[50] Yamoah, K., and P.Johnstone. Proton beam therapy: clinical utility and current status in prostate cancer. *Onco Targets and Therapy* (2014).